ACTIVE LAYER THERMAL PROPERTIES AND VEGETATION RECOVERY AT A SITE EXPERIENCING ACID DRAINAGE NEAR EAGLE PLAINS, YUKON TERRITORY, CANADA.

NICOLAS COMERFORD

Thesis submitted to the University of Ottawa
in partial Fulfillment of the requirements for the
Master of Science (M.Sc.)

Department of Geography
Faculty of Arts
University of Ottawa

Abstract

Acidic waters flowing over pyrite-rich shales are discharging near Eagle Plains, Yukon Territory, degrading the local vegetation and permafrost. Initial site investigations in 2005 found that high active layer soluble ion concentrations are likely preserving a supra-permafrost talik that recycles acidity from year to year. Using ground temperature measurements, we have determined that the loss of surface vegetation at the site has resulted in a 4°C to 6°C increase in ground surface and active later temperatures and a 1.7 to 5.1 times increase in active layer thermal diffusivity. Modeling has further shown that the change in energy balance at the ground surface accounts for the permafrost degradation at the site, and that the increased thickness of the active layer is sufficient to preserve the talik even under low salinity conditions. The thawing permafrost has however improved drainage and results in less surface runoff and improved groundwater flow that has disseminated acidity and contaminants throughout the active layer, leading to surface conditions that are more conducive to plant colonisation. Field investigations and analysis of satellite imagery demonstrate that this has reduced the surface expression of area affected by acid drainage by 53% from 2014 to 2021, and that successional changes in vegetation are occurring. Given long enough time periods, this may act as a negative feedback to permafrost degradation and allow the site to recover from past deterioration.

Acknowledgements

I would like to thank my thesis supervisor Denis Lacelle, who provided me the opportunity to do research under his supervision. Your insights in the field and in writing have proved invaluable towards my professional development over the last few years. Your knowledge of the north is inspiring and I'm sure you will continue to initiate many others to its striking landscapes.

I would also like to thank Michelle Landry and Roxanne Frappier, who assisted me during my field work and provided good laughs around the fire. I wish you both the best in your future goals. I also cannot forget Jean Bjornson for the methodological guidance provided in the lab and in the field, and for the great music suggestions, as well as Kethra Campbell-Heaton, whose comments pushed the thesis forward.

Lastly, I would like to thank my parents, David and Liette, for the immense support they have provided during my life and for kindling a curiosity to understand the world about me.

Table of Contents

List of figures

List of tables

1. Introduction

Permafrost degradation is a growing concern in the Arctic as it can induce important changes to the environment by initiating land disturbances, increasing the solute load of hydrological systems, and mobilizing carbon to microbial degradation (Lantz & Kokelj, 2008; Kokelj & Jorgenson, 2013, Séjourné et al., 2015). Degrading permafrost is generally associated with the rise in air temperatures, which increases the temperature of permafrost or lead to its thaw (Jorgenson et al, 2010). However, following surface disturbances, positive feedbacks, typically related with ponding of surface water or forest fires, can intensify thawing once initiated (Jorgenson et al., 2010; Holloway et al., 2020). Surface water generally results from the thawing of ice-rich permafrost in poorly drained soils. The lower albedo of water compared to soil and vegetation allows more incoming solar radiation to be absorbed while its high thermal conductivity facilitates heat transfer to the underlying permafrost (Loranty et al, 2018; O'Donnell et al, 2012). Forest fires also alter the surface energy balance through a series of mechanisms following the burning of the vegetation canopy and the surface organic layer. They allow more incident radiation to reach the ground surface, greater radiation absorption from decreased albedo (Amiro, 2001; Rouse, 1976) and a higher ground heat flux from exposed sediments increasing surficial thermal conductivity (Chambers & Chapin, 2002; Nossov et al., 2013). The reduction in winter canopy interception also increases the depth of the snowpack and buffers the ground surface from cold air temperatures (Jafarov et al., 2013). Although changes in the active layer hydrology and geochemistry can result in permafrost degradation following forest fires, site specific conditions lead to substantial variations in outcome (Holloway et al., 2020).

To date, the majority of studies have explored shifts in permafrost thermal regimes related to increasing air temperature, forest fires, and land disturbances associated with thermokarst processes. Few have explored them in relation with mineral resource exploitation. For instance, sedimentary exhalative (SEDEX) deposits are sulfide-rich ore bodies that are found in carboniferous shales, siltstones and carbonate rock formations (Cathro, 1982). These deposits are found over large areas of the Earth and are exploited for their rich mineral resources (Emsbo et al., 2010). The Selwyn Basin in Northwestern Canada is a notable case as it contains the second biggest reserves of global SEDEX mineral deposits (Taylor et al., 2009). However, the pyritic waste materials associated with the mining of these deposits result in acid drainage when brought into contact with atmospheric conditions (Jacobs et al., 2014). Acid drainage is a biogeochemical process that occurs from the oxidation of sulfide minerals in the presence of water and oxygen, creating acidic soil and hydrological conditions that can cause severe environmental degradation (Gray, 1996; Price, 2005). The process is ongoing as long as sulfide is available for oxidation and may occur for millennia following exposure (Jacobs et al., 2014). Its prevalence during and following mining operations has made it an important consideration to the resource extraction industry and to environmental rehabilitation efforts, who have incurred considerable costs attempting to mitigate and remediate its effects.

In the Arctic, sulfide-rich mine tailings are often buried under sediments with the assumption that permafrost will aggrade and prevent further oxidation (Meldrum 2001; Elberling 1999). Yet, there is relatively little information on the effect of acid drainage on permafrost (Jacobs et al., 2014). Studies exploring acid drainage in the Arctic generally focus on the rate of sulfide oxidation at cold temperatures (Elberling, 1999; 2001; 2005; Meldrum, 2001), on potential methods for mitigating oxidation in permafrost (Langman et al., 2017; Lessard et al., 2018) or on assessing the impact on local vegetation (Askaer et al., 2008). Lacelle et al. (2007) is the only study known to explore the effect of acid drainage on ground surface temperatures, solute cycling and active layer depths. They discovered that acid drainage induced substantial permafrost degradation, along with a recycling of soil acidity from the freezing and thawing of the active later. However, more data is needed to fully comprehend the interactions and feedbacks taking place between acid drainage, the reduction in vegetation cover and increased solute loads on permafrost thermal conditions. The growing interest in developing northern regions, especially mineral resources found in SEDEX deposits, underlies the importance of understanding the thermal response of permafrost to acid drainage, which will be useful to resource developers looking to mitigate environmental degradation associated with acid drainage induced permafrost thaw.

As such, the objective of this thesis is to examine the effect of acid drainage on the ground thermal regime at a site near Eagle Plains, YT. At this site, acid drainage was initiated following the excavation of material for the construction of the Dempster Highway in the 1970s, inducing the deterioration of the vegetation cover and the underlying permafrost and precipitating iron-minerals at the surface (Lacelle et al., 2007; 2010). The objective of this thesis is achieved by: (1) determining the spatial extent of the area affected by acid drainage and its effect on vegetation using satellite imagery, the NDVI index and field investigations; (2) determining the thickness of the active layer and the concentration of solutes and comparing them with measurements from 2005; and (3) exploring the effects of acid drainage on active layer temperature, moisture and salinity using 3-in-1 soil sensors placed through the soil profile. Measurements and samples are collected from both the area affected by acid drainage and the adjacent non-affected forest, which is used as a control site. The results from the study will determine the thermal impact of acid drainage on permafrost and the potential feedbacks that are taking place.

2. Literature Review

2.1 Acid drainage

Acid drainage is a biogeochemical process wherein iron sulfide minerals, typically pyrite, are exposed to water and oxygen, initiating oxidation and the release of iron (Fe^{2+}) and hydrogen (H^{+}) ions in solution (Jacobs et al., 2014). Though commonly associated with mine waste material, acid drainage also occurs naturally in many locations. The ions released following oxidation decrease the pH of affected waters, leading to detrimental conditions for most organisms when the pH decreases below 5.5 (Jacobs et al., 2014). The excess acidity also reacts with local minerals, affecting the mobility, leachability and bioavailability of metals and trace elements such as aluminum, cadmium, copper, magnesium, nickel and zinc (Price, 2005). In high concentrations, these elements negatively affect the physiology of organisms. Together, both the high acidity and the elemental composition of areas affected by acid drainage can result in zones of stressed and stunted vegetation or in extreme cases, zones devoid of vegetation altogether (Gray, 1996).

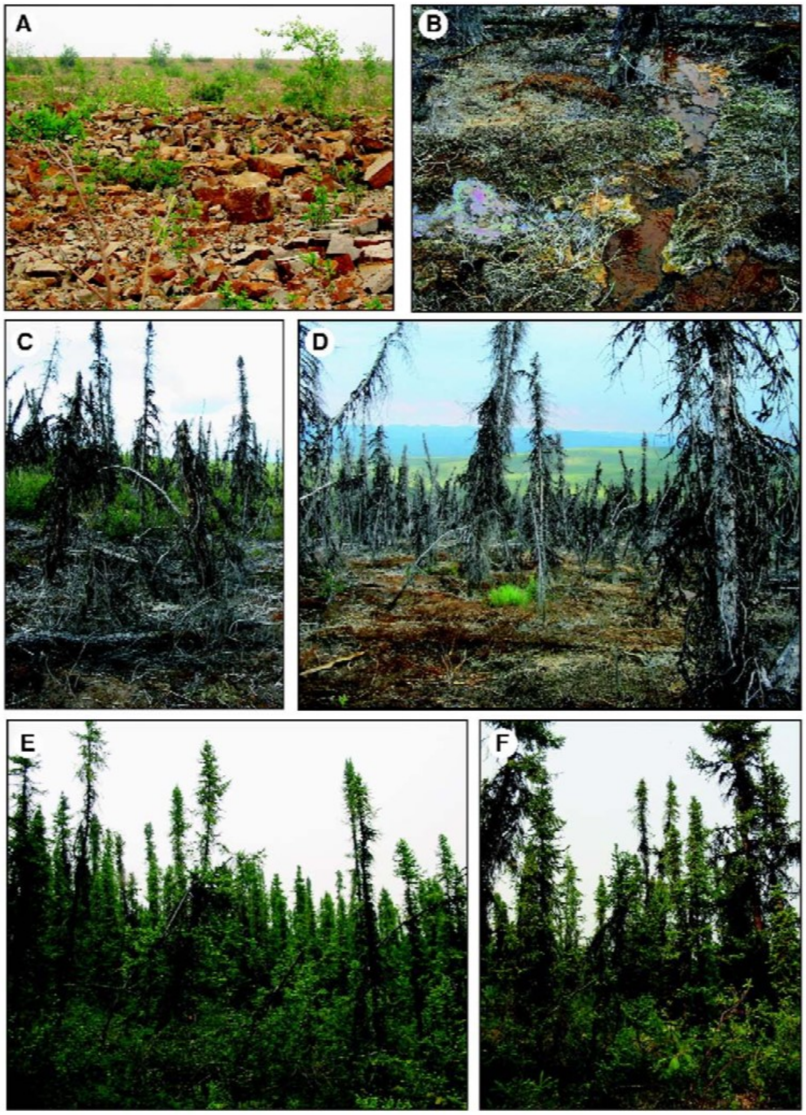

Figure 1. Field photographs of: A–B) the excavated area. C–D) the area affected by acid drainage; E–F) the adjacent non-affected landscape, near Eagle Plains, northern Yukon Territory (from Lacelle et al., 2007).

2.1.1 Sulfide oxidation

Sulfide (S^{2-}) is an inorganic anion of sulfur that can often be bound in compounds and is naturally abundant in iron sulfide minerals (FeS_2). The oxidation of sulfide is part of the global sulfur cycle as it allows the exchange of sulfur between the lithosphere and hydrosphere (Jacobs et al., 2014). The process occurs through a series of redox reactions requiring both oxygen and water to catalyze:

$$2FeS_2 + 7O_2 + 2H_2O \rightarrow 2Fe^{2+} + 4SO_4^{2-} + 4H^+ \qquad \text{(Eq. 1)}$$

$$4Fe^{2+} + O_2 + 4H^+ \rightarrow 4Fe^{3+} + 2H_2O \qquad \text{(Eq. 2)}$$

$$2Fe^{3+} + 6H_2O \rightleftharpoons 2Fe(OH)_3 + 6H^+ \qquad \text{(Eq. 3)}$$

$$14Fe^{3+} + FeS_2 + 8H_2O \rightarrow 15Fe^{2+} + 2SO_4^{2-} + 16H^+ \qquad \text{(Eq. 4)}$$

$$FeS_2 + 7Fe_2(SO_4)_3 + 8H_2O \rightarrow 15FeSO_4 + 8H_2SO_4 \qquad \text{(Eq. 5)}$$

Equation 1 demonstrates how iron sulfide is oxidised to release sulfate as well as hydrogen (H^+) and ferrous iron (Fe^{2+}) ions, reducing the pH of the solution. The hydrogen ions also combine with sulfate (SO_4^{2-}) to produce sulfuric acid (H_2SO_4). In the presence of oxygen (Eq.2), ferrous iron is further oxidised into ferric iron (Fe^{3+}), which can precipitate into ferric hydroxide [$2Fe(OH)_3$], a characteristics by-product of sulfide oxidation, in a reversible precipitation-dissolution reaction (Eq.3). The ferric iron can also react with additional iron sulfide to release more ferric iron and hydrogen ions (Eq.4), further increasing the acidity of the solution. As iron sulfide continues to oxidise, increasing amounts of sulfuric acid is generated (Eq.5) (Jennings et al., 2008).

Although theses reactions occur abiotically, the presence of acidophilic iron- and sulphur-oxidizing micro-organisms increases the oxidation rate by several orders of magnitude (Figure 2) (Nordstrom & Southam, 1997). They derive energy as electrons are transferred from an electron-donor to an electron-acceptor, namely in an aerobic process as H^+ ions transfer electrons to oxygen molecules looking to fill their outer valance ring (Jacobs et al., 2014). The reaction is exothermic is nature, releasing approximately 40kcal/mol of oxidised ferric iron and 150kcal/mol of oxidised sulfide. The difference stems from the number of electrons transferred, as the oxidation of sulfide into sulfate takes 8 electrons while the oxidation of ferrous iron into ferric iron takes 1 electron. As such, iron-oxidizing bacteria need to convert large quantities of iron to meet their energetic requirements, producing a substantial amount of ferric oxyhydroxide in the process and making it difficult to stop acid drainage once it has been initiated (Chapelle, 1993).

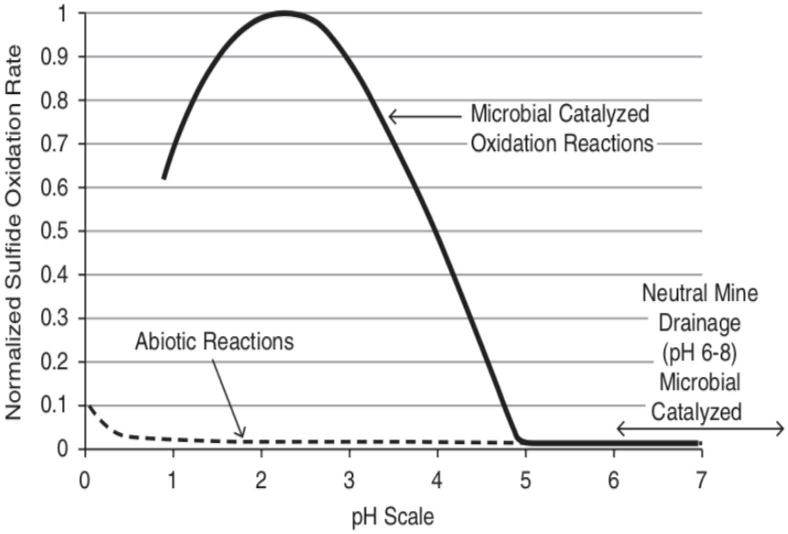

Figure 2. Microbially catalyzed rates of sulfide oxidation in relation to abiotic oxidation (from Jacobs et al., 2014).

2.1.2 Controls on sulfide oxidation

The rate of sulfide oxidation is strongly regulated by temperature and pH, as low temperatures and high pH values slow chemical reaction rates and decrease microbial activity (Schoonen et al., 2000; Meldrum et al., 2001). The micro-organisms associated with acid drainage thrive in environments where pH values are less than 3, exponentially increasing the rate of oxidation from more alkaline conditions (Figure 2). Certain bacteria are found at more neutral pH values, though their effect on the rate of oxidation is minimal (Jacobs et al., 2014). Optimal temperatures for bacterial activity associated with sulfide oxidation are > 20°C. (Jacobs et al., 2014). It is possible that certain species have adapted to proliferate at lower temperatures as characterisation of arctic bacteria is incomplete, however freezing conditions are known to limit biological activity.

Saturated and frozen soil conditions are known to limit oxidation, as the rate of oxygen diffusion through air (10^{-5} m^2 s^{-1}) is four orders of magnitude higher than through water (10^{-9} m^2 s^{-1}) and six orders of magnitude higher than through ice (10^{-11} m^2 s^{-1}) (Fredlund et al., 2012, Elberling, 1999). Under unsaturated conditions, important oxidation in the soil column occurs as long as atmospheric oxygen can diffuse into the soil profile (Eberling, 2005). Barring freezing conditions, this is a factor of the grain size distribution of the soil, as fine-grained sediments have less pore cavity space to allow the free movement of gases. The formation of a ferric oxide precipitate crust at the oxidation boundary may further limit diffusion (Eberling, 2005). Under freezing conditions, the potential for oxidation is likely found as long as liquid water is present, although it has been proposed that increasing ice formation during freezing prevents the free movement of oxygen in sediments, and as such may further limit the potential for oxidation to occur as temperatures drop (Elberling, 2005).

Although sulfide oxidation rates are more important during the warm season, experimental results indicate that the cold season may account for up to 40% of annual oxidation (Eberling, 2001). This is consistent with the seasonal cycling rates of carbon (Fahnestock et al., 1998) and nitrogen (Brook et al, 1997).

2.2 Sedimentary Exhalative deposits

Sedimentary Exhalative (SEDEX) deposits are sulfide-rich ore bodies that are found in sedimentary basins containing carboniferous shales, siltstones and carbonate rocks (Cathro, 1982), and are characterised by the presence of pyrite. They form under marine conditions in proximity to rift systems where sulfide minerals precipitate from the mixing of brine and hydrogen sulfide locally produced by bacterial or thermochemical reduction of sulfate in seawater (Emsbo et al., 2010). They are thought to be genetically related to Mississippi Valley Type (MVT) deposits, which are often found in close proximity and contain a similar mineral composition (Goodfellow et al., 1993). These deposits however differ in that they result from the replacement of carbonates below the seafloor following the migration of brine solutions to carbonate platforms (Nelson et al., 2002). Galena (PbS) and sphalerite (Zn,Fe)S are the principal ores produced in these deposits, and as such are commercially important given their high concentrations of lead, zinc and silver minerals (Emsbo et al., 2010).

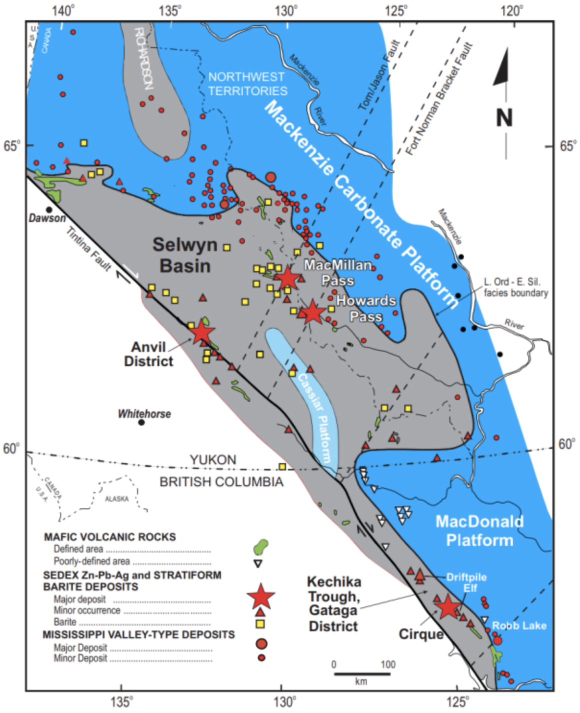

Figure 3. The Selwyn basin of northwestern Canada and associated SEDEX and MVT deposits (from Goodfellow et al., 1993).

2.3 Permafrost

Permafrost is a ubiquitous component of polar and high alpine environments. It is defined as ground that remains perennially cryotic (< 0°C) for at least 2 consecutive years (French, 2018). The presence of factors such as ions and pressure create conditions where water can be found at ground temperatures below 0°C, thus permafrost isn't necessarily entirely frozen. The thickness of permafrost is grossly determined by conductive heat generated by geothermal energy and from net radiation balance at the ground surface (French, 2018). The latter is controlled by interactions between snow cover, vegetation, topographic aspect and surficial sediments (Gray & Brown, 1979). Snow is an effective insulator, buffering the ground surface from cold air temperatures, leading to less top-down freezing during the winter (French, 2018). Vegetation provides shade and insulates the soil from incoming radiation during the summer (Shur & Jorgensen, 2007). Shrubs and other deciduous vegetation capture windblown snow during the winter, insulating the ground from cold temperatures. Conversely, the canopy of evergreen trees capture snow, resulting in less ground surface snow accumulation. Topographic aspect control's the amount of solar insolation received at the ground surface as well as the depth of the snowpack due to the orientation of slopes relative to the sun and to local dominant winds (Gorbunov, 1978). The type of surficial sediments and ice content control the thermal conductivity of the soil and the physical processes that affect hydrological fluxes within the ground (French, 2018).

2.3.1 Ground ice

Ground ice is an important component of permafrost, though it is not always found within it. It occupies pores, cavities and voids in the ground, and as such is common in unconsolidated materials (French; 2018). Ground ice genesis is regulated by ground temperatures, active layer moisture, and by the quantity of unfrozen water within permafrost (French, 2018; Fisher et al., 2020). The former parameters are a factor of the local climate, while the latter also factors in the physical characteristics of the soil as well as the type and concentration of solutes in interstitial water, which lower the freezing point depression. Fine-grained sediment, which has a higher specific surface area than coarse sediment, can hold larger quantities of water under surface tension as Van der Waals attractions bond mineral or organic particle surfaces with liquid water (Williams & Smith, 1989; Anderson et al., 1973). As such, fined-grained sediments are deemed frost susceptible and segregated ice and excess ice typically develops within them. Pore ice is typically found in coarse-grained sediments that cannot hold as much residual unfrozen water.

The vertical distribution of ground ice is variable, however the highest concentrations are predominantly found in the transient layer and the first 2 meters of permafrost (Williams, 1968; Kokelj & Burn, 2005). This is due to the effects of capillarity which allows the migration of water towards the freezing front following thermal and pressure gradients, otherwise known as cryosuction (French, 2018; Fisher et al., 2020). As such, active layer moisture migrates downwards towards the base of permafrost during the warm season, and to a lesser extent, smaller quantities of unfrozen water within permafrost migrates upwards during the cold season. Moreover, the seasonal movement of water within permafrost is limited as top-down ice growth occurs, progressively leading to the creation of other ice-rich zones that increase in content over time (Fisher et al., 2020). Under non-equilibrium conditions, these ice-rich zones can act as a buffer to permafrost degradation due to the latent heat required to convert ice to water (Fisher et al., 2020).

2.3.2 Acid drainage in permafrost environments

Though commonly studied in temperate regions, acid drainage remains poorly studied in periglacial regions. Recent investigations are however making an association with increasing temperatures and rising solute concentrations in periglacial lakes and streams as glaciers and other cryotic landforms melt and permafrost thaws (Kolkejv et al., 2013; Salerno et al., 2016; Skovsholt et al., 2020). Further, the solute flux from meltwaters passing over newly exposed earth materials can be strongly supplemented by carbonate dissolution and sulfide oxidation (Anderson et al., 2000), indicating that thawing permafrost may be a catalyst for naturally occurring acid drainage.

Evidence is found in alpine lakes surrounded by permafrost containing sulfide rich minerals, where lacustrine acidity has been increasing as permafrost thaws with rising temperatures (Ilyashuk et al., 2018). A marked increase in acidity is observed when MAATs are over -2°C and groundwater persists under liquid form for most of the year, though it is also likely a factor of the freezing point depressions associate with solute concentrations.

The solutes and acidity leached into the soil due to acid drainage can be recycled from year to year during the winter freeze back of the active layer (Lacelle et al., 2007; 2010). Fe-hydroxide, Fe-sulfate and Ca-sulfate minerals precipitate during freezing as the solution saturates ahead of the freezing front, releasing H^+ and forming sulfuric acid. This acidity remains over winter in supra permafrost taliks or as residual water and is released in the spring thaw to potentiate a more extensive rate of silicate dissolution and the release of trace metals (Figure 4). The precipitation of Fe-Ca minerals during freezing further leads to a different solute composition (Cl-Mg-Na-SO4 geochemical facies) than occurs during evaporation (Fe-Mg-SO4 geochemical facies) (Lacelle, 2010). As such, acid drainage occurring in periglacial regions creates distinctive geochemical conditions compared to acid drainage occurring in temperate and tropical regions.

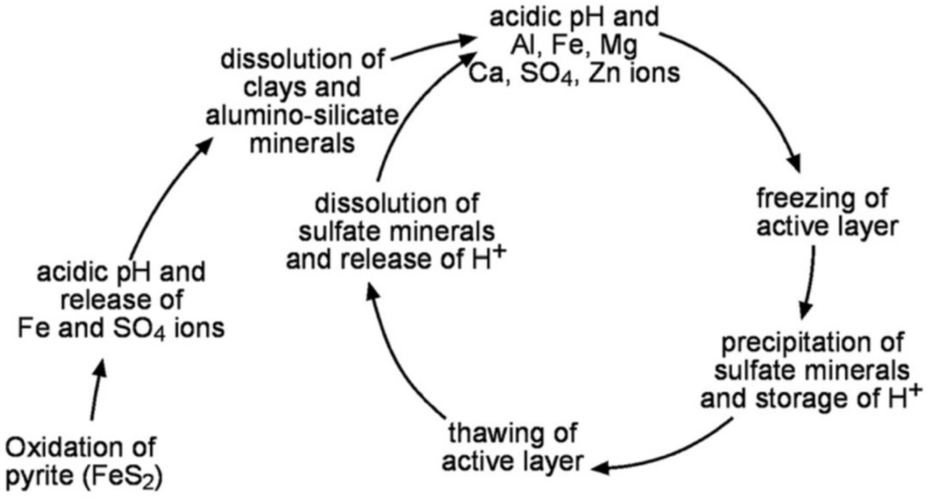

Figure 4. Proposed sequence of origin of acid drainage and recycling of acidity at Eagle Plains, northern Yukon Territory (from Lacelle et al. 2007).

3. Study Area

3.1 Regional setting

Eagle Plains (66.37095°N, 136.72044°W) is found within the Eagle Plains ecoregion, an intermontane basin of Devonian through Cretaceous sedimentary rocks bordered by the Richardson, North Ogilvie and Dave Lord mountain ranges (Smith et al, 2004). The region consists of low relief rolling hills primarily found between 300m and 600m above sea level (asl), although the highest peaks extend over 1000m asl. The northward flowing Porcupine river, and its main tributaries the Eagle and Whitestone rivers, drain the majority of the basin, while the Peel, Ogilvie and Wind rivers drain the southwestern portion. The Dempster highway, a 737km long gravel road joining the communities of Dawson (YT) and Tuktoyaktuk (NWT) runs roughly N-S through the heart of the region.

The region is part of the continental sub-arctic climatic zone, which is characterised by long, cold winters and short summers. The mean annual temperature in the region is -7.5°C, with annual precipitation totalling 400mm (Smith et al., 2004). These conditions favour vegetation characterised by spruce woodlands, with an understory of shrub birch, willow, alder, Labrador tea, mosses and lichens (Murray, 1997). The climate also places the region within the southern limit of the continuous permafrost zone, where permafrost may reach depths of 200m. Ground ice is common along the Dempster Highway (EBA, 1990), and important accumulations of segregated ice may be found in near-surface permafrost (Micheal, 1983). In fine grained, poorly drained soils, patterned ground formed by ice wedge polygons also occurs (Thomas & Rampton, 1982).

The presence of the Richardson mountains to the east of the study area prevented the advance of the westward flowing Laurentide ice sheet, and the area remained unglaciated throughout the Wisconsin glaciation (Figure 5). As such, colluvium is predominantly found in near-surface sediments, with alluvial deposits along river valleys (Smith et al, 2004). Glaciolacustrine and glaciofluvial deposits are however found where glacial meltwater from bordering mountain ranges flowed into the region. The Laurentide ice sheet also prevented the outflow of the eastward draining Peel river, forming glacial lake Hughes and diverting outflow northwards through the Eagle River discharge channel into the Porcupine river and glacial lake Old Crow (Duk-Rodkin & Hughes, 1995).

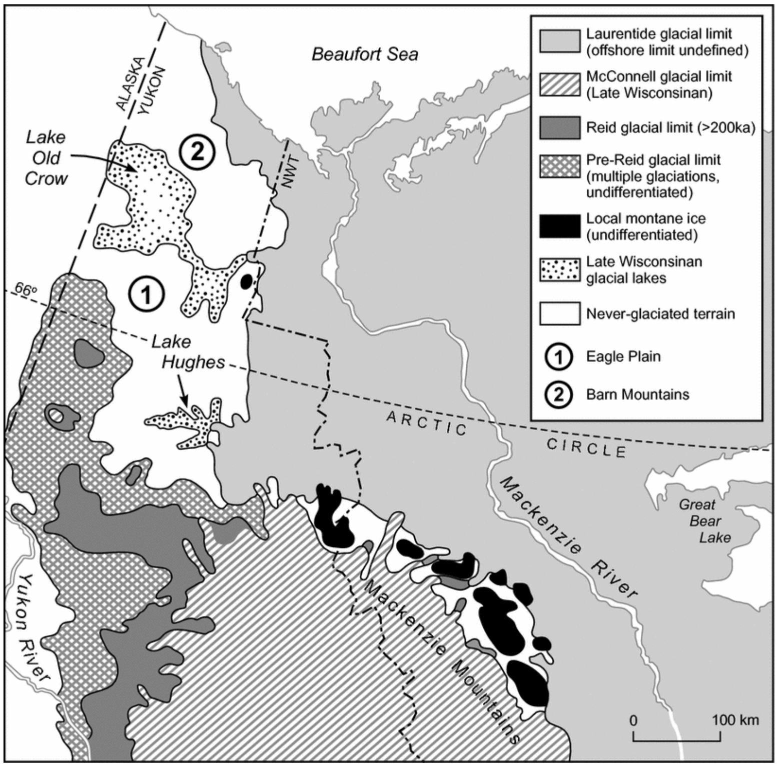

Figure 5. Glacial setting of the northern Yukon and the Eagle Plains ecoregion (Taken from French, 2017).

3.2 Study Site

Acid drainage was observed to occur over an area approximately 500m by 100m wide directly southeast of a large excavation atop which sits Eagle Plains Lodge (Figure 7). The excavation of surface materials used for the construction of the Dempster highway in the 1970s exposed the underlying pyrite-rich shales to atmospheric water and oxygen, inducing extensive acidification of a local intermittent stream and the surrounding soil (Lacelle et al. 2007). Iron oxide tinted soils coupled with stressed and deteriorating vegetation are indicative of the areal extent of acid drainage (Figure 6). Based on trace metal concentrations in tree rings from the affected area, Doucet (2006) suggested that acid drainage initiated in 1970, which corresponds to an increase in trace metal content. The intermittent stream that flows through the area affected by acid drainage originates from the excavated area and flows downslope from an elevation of approximately 720 meters asl to 360 meters asl where it discharges into a tributary of the Eagle river.

Figure 6. Effects of acid drainage on vegetation and surface expression at Eagle Plains, August 2021. The red coloration is ferrihydrite accumulation from the high iron concentrations associated with acid drainage.

The bedrock at Eagle Plains is composed of Upper Devonian shales and sandstone overlain by lower Carboniferous shales, sandstone and conglomerates of the Ford lake formation (Norris, 1975). Unconsolidated colluvium of rock fragments, sand and silt typical of unglaciated environments overlies these formations. The granular distribution of the soil within and directly outside of the affected site is characterised as silty loam, composed predominantly of sand (65%) and clay (30%) (Lacelle et al., 2007). Recorded mean annual air temperatures at the Eagle Plains meteorological station (720 m asl) are -4.1°C ± 3.8°C, with a mean monthly high of 14°C in July and low of -19.3°C in January (Environment Canada, 2004). Annual precipitation is moderate, averaging 380 mm per year and mostly falling as rain during the summer months. Vegetation is dominated by black spruce, with grasses, mosses, lichens and shrubs in the understory (Doucet et al., 2006; Lacelle et al, 2007). The local permafrost thickness is estimated to reach a depth of 61m (Lacelle et al., 2007).

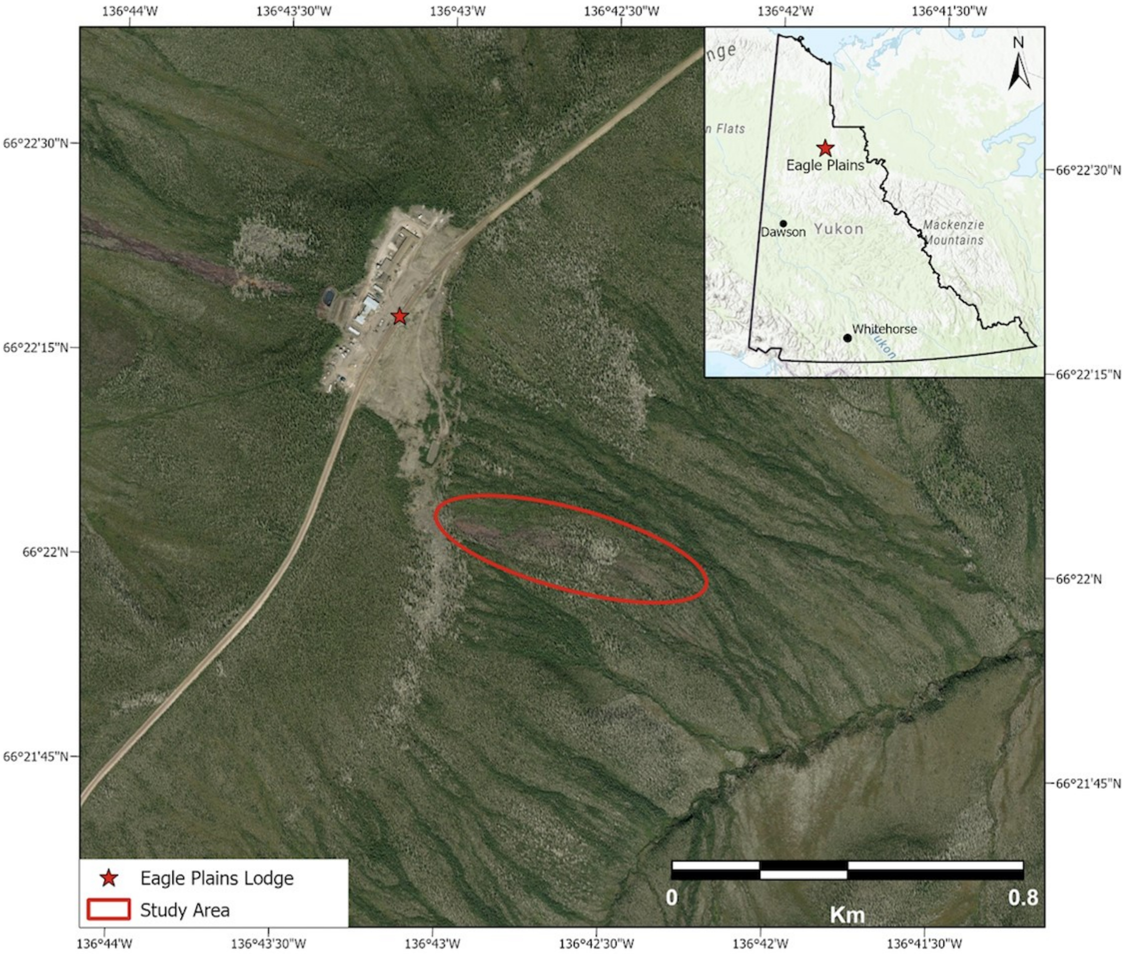

Figure 7. Location of the study area in relation to Eagle Plains Lodge.

4. Methodology

4.1 Field Sampling

The study site was visited from August 7th – 9th 2021. Conditions at the time were cool and overcast with intermittent periods of rain. The site affected by acid drainage had dry soil conditions and no standing water was found on site, making water sampling impossible. Transects running the length of the area affected by acid drainage and in the adjacent forest were conducted at 25m intervals to sample permafrost depths using a frost probe and acquire pictures and coordinates for ground-truthing data of surface conditions (Figure 8). The percent vegetation cover was recorded in 1m x 1m plots using a scale of 1 to 5, where 1 represents 0 - 20% vegetation cover and 5 represents 80 - 100% cover (Kutiel et al. 1998). The main plant functional types were also recorded to establish a measure of community complexity using a methodology similar to Sulman et al. (2021), which differentiates plant functional types based on plant lifecycles, ecosystem function and community structure.

Two pits were dug in the area affected by acid drainage in an attempt to reach the top of permafrost (Figure 8), one near the ephemeral stream outlet (AS1: coordinates 66.36738°N, 136.71532°W) and one approximately 200 m downslope (AS2: 66.36715°N, 136.71126°W). A layer of rubble found at a depth of 90 cm however prevented further digging into the active layer. Sediment samples from the pits were taken at 5 cm intervals and double bagged in heavy-duty Ziploc bags to be taken back to the University of Ottawa for further analysis. Four Decagon 5TE 3-in-1 temperature/salinity/moisture sensors were installed at depths of 10, 25, 50 and 75 cm at both sites to collect hourly measurements of seasonal ground temperatures, salinity and moisture flux rates before refilling the pits with the extracted sediment. The sensors have an accuracy of ±1°C for temperature, ± 3% for moisture and ± 10% for salinity (METER group, 2019). Two more pits were dug in the forest adjacent to each site in the affected area until the top of permafrost was reached, and sediment samples taken at 15cm intervals. Loggers were left for a period of a period of 8 months until their retrieval on March 16th 2022. Data from a previous field excursion in 2008 was also used to analyse changes in active layer depths and temperatures between both time periods. Sensors were installed for a period of one year from July 2008 to August 2009. Snow depths were also calculated at this time using an average of 10 measurements at each site. Two sites were similarly sampled in the adjacent forest in the unaffected area.

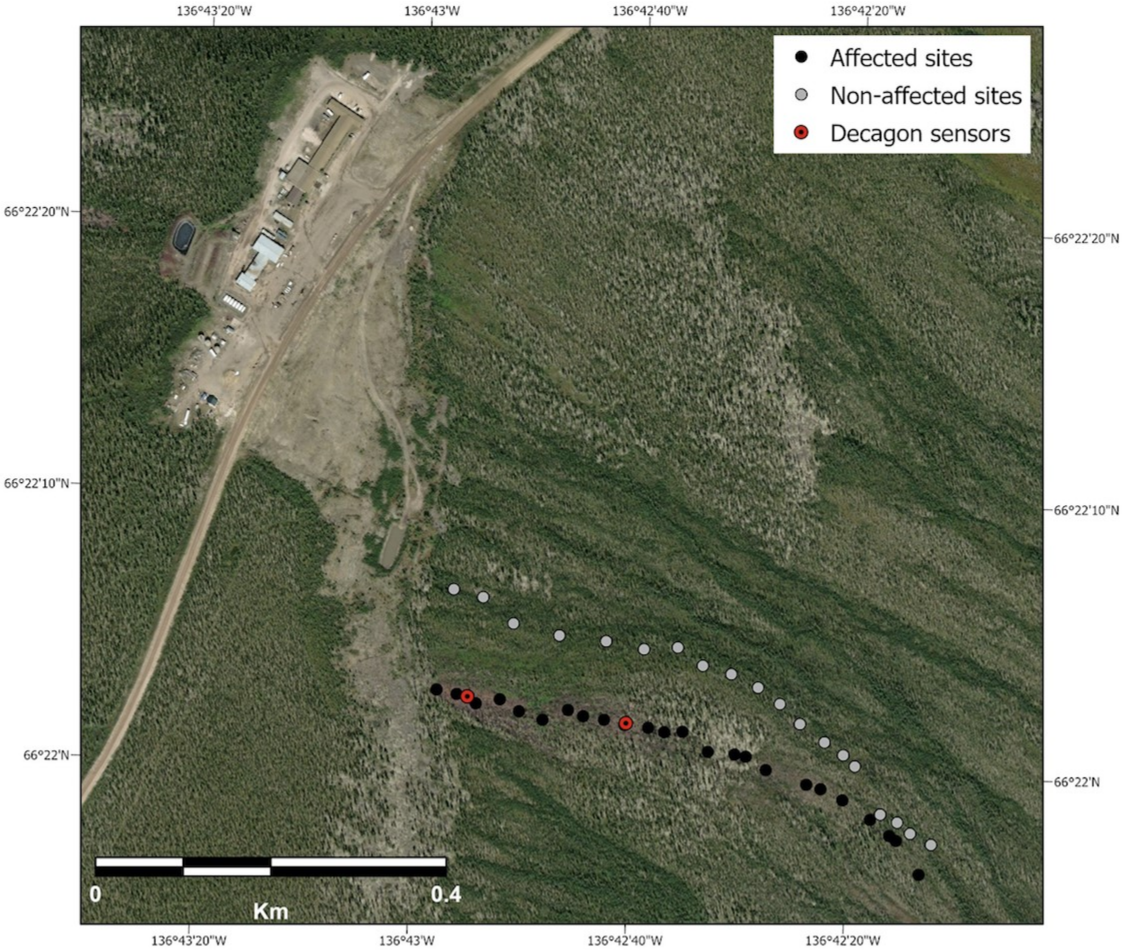

Figure 8. Location of the sampling sites in the area affected by acid drainage and the adjacent non-affected forest in August 2021. The excavated area can be seen to the west and north of the site affected by acid drainage along with Eagle Plains lodge.

4.2 Supervised Classification

Two satellite images of the Eagle Plains area, taken on June 18th 2014 and July 15th 2021, were acquired from Digital-Globe's Worldview-2, which takes 8-band multispectral images at a resolution of 1.84 m and a pan-chromatic image at a resolution of 0.74 m. The pan-sharpened images of the site were used to determine the change in the area affected by acid drainage between 2014 and 2021 using pixel-based supervised classification. Classification of the area of interest was split between 5 classes that were observed in the field and in satellite imagery: forest, rock rubble, lichen, meadows and acid drainage affected terrain. Polygons for training data were created using the 2021 imagery and the same training areas were applied to 2014 imagery. The chosen classifier was a Support Machine Vector using a maximum of 5000 samples per class. Classified images were post-processed in ArcGIS using the *Majority Filter* tool with a neighbourhood of 8 cells (3x3 window) to homogenise isolated cells using surrounding values and the *Boundary Clean* tool using an ascending sort type to smooth boundaries between different classes. Following, the *Region Group* tool was applied to classify all individual groups of cells and the *Set Null and Nibble* tools used to replace all groups with under 50 cells using the nearest neighbour values. This represents an area approximately 5 m x 5 m. The final output smooths out the classification scheme and reduces the amount of "peppering" in the map, where individual or small groups of cells of any class are spread throughout the area of interest.

Since the rubble and lichen classes often co-occurred and their distinguishment from each other unnecessary for the purposes of this study, they were merged into the same class. The final classification was evaluated using a confusion matrix of 24 sample points taken during field work to assess its accuracy. The rasters were converted to polygons and clipped to the boundary of the watershed to calculate the change in surface area of each class for both years.

To quantify the change in surface area for classes at the site from 2014 to 2021, the basins for the 2 ephemeral creeks that discharge the area we're computed in ArcGIS using the Polar DEM and the watershed toolkit. Although field investigations seemed to show that the site was drained by only 1 creek, the watershed it delineated in ArcGIS did not cover the whole portion of the acid drainage site. As such, a second creek was added to the watershed to effectively cover the affected area. This difference might be due to the limitations of effectively delineating a watershed at such a large scale using reductive flow direction and accumulation techniques as are available in the watershed toolkit. The watershed was artificially cut off on the western side just beyond the outlet of the ephemeral stream since the area was excavated for surface materials and does not comprise the forested area affected by acid drainage.

4.3 Vegetation activity

The negative impacts of acid drainage on vegetation are well known, where it leads to growth inhibition, reduction of foliar cover and mortality (McBride, 1994; Siegel, 2002). Field spectroscopy has been proposed as an effective means of monitoring the effects of acid drainage on plant health using the Normalized Difference Vegetation Index (NDVI) (van Deventer & Cho, 2014). NDVI is an index that quantifies greenness based on the fact that chlorophyll absorbs red light while the cellular structure of leaves strongly reflects near-infrared (NIR) wavelengths (Petrolli, 2013). When the cellular structure is deteriorated, its potential to absorb the NIR decreases. As such, the ratio of change between red and NIR light is indicative of the presence of chlorophyll and plant cellular damage. NDVI is calculated as follows:

$$NDVI = \frac{NIR - Red}{NIR + Red} \qquad \text{(Eq. 6)}$$

To further assess the results of the supervised classification, the NDVI for both images was calculated and the difference between both periods was determined as:

$$NDVI_{diff} = NDVI_{2021} - NDVI_{2014} \qquad \text{(Eq. 7)}$$

Since the satellite images are taken at different months in summer (June 18th 2014 and July 15th 2021), an analysis of the change in NDVI for the meadow class, which should see the most natural change in NDVI values from spring to summer, was assessed by comparing the change in NDVI for meadows within the watershed to the change in NDVI for meadows within a square polygon encompassing but excluding the watershed. Welch's T-test, a version of the t-test used for samples having unequal variances and unequal sample sizes, was used to determine if the difference in means is statistically different. The test was performed in R statistical software.

4.4 Ground temperatures and thermal diffusivity

Sensors for the Decagon data logger failed at 10 cm depth at AS1, and also at 50 cm depth at AS2, while salinity measurements failed at all sensors save at 10 and 75 cm depth at AS2. Hourly measurements were converted to daily averages to investigate temperature, moisture and salinity fluxes in the active layer and temperature measurements used to calculate the thermal diffusivity of the soil column. The thermal diffusivity (D) is a measure dependant on soil properties, and is calculated as:

$$D = \frac{k}{pC} \qquad \text{(Eq. 8)}$$

where k = thermal conductivity, p = soil density and C = specific heat capacity of the selected materials. It is a measure that can be highly variable within soil column as it changes with grain size, mineralogy, density, moisture and phase changes, and as such is difficult to accurately calculate. Methods have however been developed to approximate the thermal diffusivity of a soil column using a known temperature field by numerically computing the time derivative and second-order space derivative in the heat conduction equation:

$$\frac{\partial T(z,t)}{\partial t} = D\frac{\partial^2 T}{\partial z^2} \qquad \text{(Eq. 9)}$$

where $T(z,t)$ is the temperature (K) at depth z(m) and t(s) and where D is the apparent thermal diffusivity ($m^2\ s^{-1}$). When temperature sensors are placed at unequal intervals in the soil column, the equations to calculate the finite differences change to:

$$\frac{\partial T(z,t)}{\partial t} = \frac{T(z,t+\Delta t)-T(z,t-\Delta t)}{2\Delta t} \tag{Eq. 10}$$

and

$$\frac{\partial^2 T(z,t)}{\partial z^2} = \frac{\frac{T(z+\Delta z_2,t)-T(z,t)}{\Delta z_2}-\frac{T(z,t)-T(z-\Delta z_1,t)}{\Delta z_1}}{\frac{\Delta z_1+\Delta z_2}{2}} \tag{Eq. 11}$$

This method assumes that the thermal properties of the soil are constant over time and space (Pringle et al., 2003; Marinova et al., 2022). However, it should be noted that this approach suffers difficulties when the temperature curvature, $\partial^2T/\partial z^2$, passes through zero (Zhang and Osterkamp, 1995), and it requires temperature measurements with an accuracy comparable to their precision. The apparent thermal diffusivity may be more accurately presented using the geometric mean slope of the time and second-order space derivatives (D_{geo}), which is calculated by dividing the slope of the time vs the space derivative (D_{norm}) by the slope of the space vs the time derivative (D_{inv}). This smooths out measurement errors and makes results more directly comparable between sites. This graphical approach was previously applied to sea ice measurements (McGuinness et al., 1998; Trodahl et al., 2000, 2001)

4.5 Laboratory analysis

The grain size distribution of soil samples was determined using a Microtrac Particle Size Analyzer (Department of Geography, Environment and Geomatics, University of Ottawa) following drying and sample immersion in three 24h treatments of hydrogen peroxide to remove organic material. Soil pH was measured by adding 5 grams of sediment < 2mm to an Erlenmeyer flask containing 50ml of distilled water and shaking the mixture for 1 hour. The mixture was subsequently filtered through a 45 µm pore diameter filter and a Fisher Accumet 610A pH meter used to measure the pH values (Girard et al., 2003).

Active layer soluble ions were leached from the sediment samples by soaking 5g of sediment in 50 ml of distilled water and shaken for 1-hour before being centrifuged and decanted in the laboratory. The water was then filtered with 0.45 microns filters, and the soluble anion (Cl^-, SO_4^{2-},NO_3^-) concentrations were measured using Ion Chromatography and soluble cation (Al_{tot}, Ca^{2+}, Fe_{tot}, K^+, Mg^{2+}, Mn_{tot}, Na^+ and Zn^{2+}) concentrations measured using an Inductively Coupled Plasma Atomic Emission Spectrometer (ICP-AES) at the Geochemistry Laboratory, University of Ottawa. Analytical reproducibility is ± 5%.

5. Results

5.1 Remote Sensing

Results from the supervised classification confirm visual observations of satellite imagery that acid drainage affected area has decreased between 2014 and 2021 (Table 1, Figure 9). The area affected by acid drainage has reduced from 11 686 m^2 in June 2014 to 5 534 m^2 in July 2021, a 53% decrease in surface area. Most of the changes took place in the central section of the affected area. Meadows, which in this area are typically associated with terrain recovering from the effects of acid drainage as vegetation re-colonises the surface, have also decreased in surface area within the watersheds from 30 918 m^2 in 2014 to 27 583 m^2 in 2021, an 11% change. While this can be attributed to forest expansion into previous meadow areas, the full growth of vegetation has likely not occurred by mid-June and is likely an important factor to consider. Nonetheless, given the predominance of spruce trees in area, the change in leaf cover would for the most part be found in shrubs and small plants, which would be more important to the spectral signature of meadows than the forest class with its evergreen canopy and ground moss cover. Analysis of the change in NDVI from 2014 to 2021 support evidence from the classification that the area affected by acid drainage is decreasing and that successional changes in vegetation are occurring (Figure 10) since the majority of the greening is occurring within the limits defined by both classes within the watershed. The difference in mean NDVI values for meadows within the watershed (0.0561 ± 0.091, n = 2578) to meadows just outside (0.0186 ± 0.098, n = 5331) was statistically significant ($p < 0.01$) within a 99% confidence interval, indicating that the change in greening cannot be attributed to differences in monthly NDVI values alone.

The accuracy of the classification was calculated using a confusion matrix of ground truth points running in transect through the affected area (Table 2). Out of 24 points, 19 were correctly classified, giving the classification an accuracy of 79%. It was found that acid drainage affected terrain and rubble/lichen were under classified, with the classifier having poor sensitivity to the latter, while forest and meadow were over classified. This is likely an effect of the post processing, as the smoothing tends to preserve classes that are well-connected throughout the image and reduce or eliminate classes that are sporadic and of individual pixels (Table 1). While the accuracy of the classification is the same even without post-processing, the proximity of patches reflecting the true conditions, namely regarding the presence of acid drainage and rubble/lichen, is close enough to warrant error simply based on source image accuracy (Worldview-2 = 5m) and GPS point accuracy (Garmin GPS = 15m). The results of the accuracy assessment may therefore be due to limitations at classifying large-scale images in heterogenous terrain.

Table 1. Areal extent of classes categorized under supervised classification.

Year	**Class**	**Area pre-processing (m^2)**	**Area post-processing (m^2)**
2014	Forest	151 036	153 669
	Rock Rubble/Lichen	2 999	2 906
	Acid Drainage	12 140	11 686
	Meadows	33 006	30 918
2021	Forest	157 263	164 826
	Rock Rubble/Lichen	2 014	1 243
	Acid Drainage	6 280	5 534
	Meadows	33 629	27 583

Table 2. Confusion matrix showing accuracy of the supervised classification model.

		Ground-truth				
		Forest	Rubble/Lichen	Acid Drainage	Meadow	Precision
Predicted	Forest	4	1	2	0	57.14 %
	Rubble/Lichen	0	1	0	0	100.00 %
	Acid drainage	0	0	10	0	100.00 %
	Meadow	0	1	1	4	66.67 %
	Sensitivity	100.00 %	33.33 %	76.92 %	100.00 %	**Accuracy** 79.17%

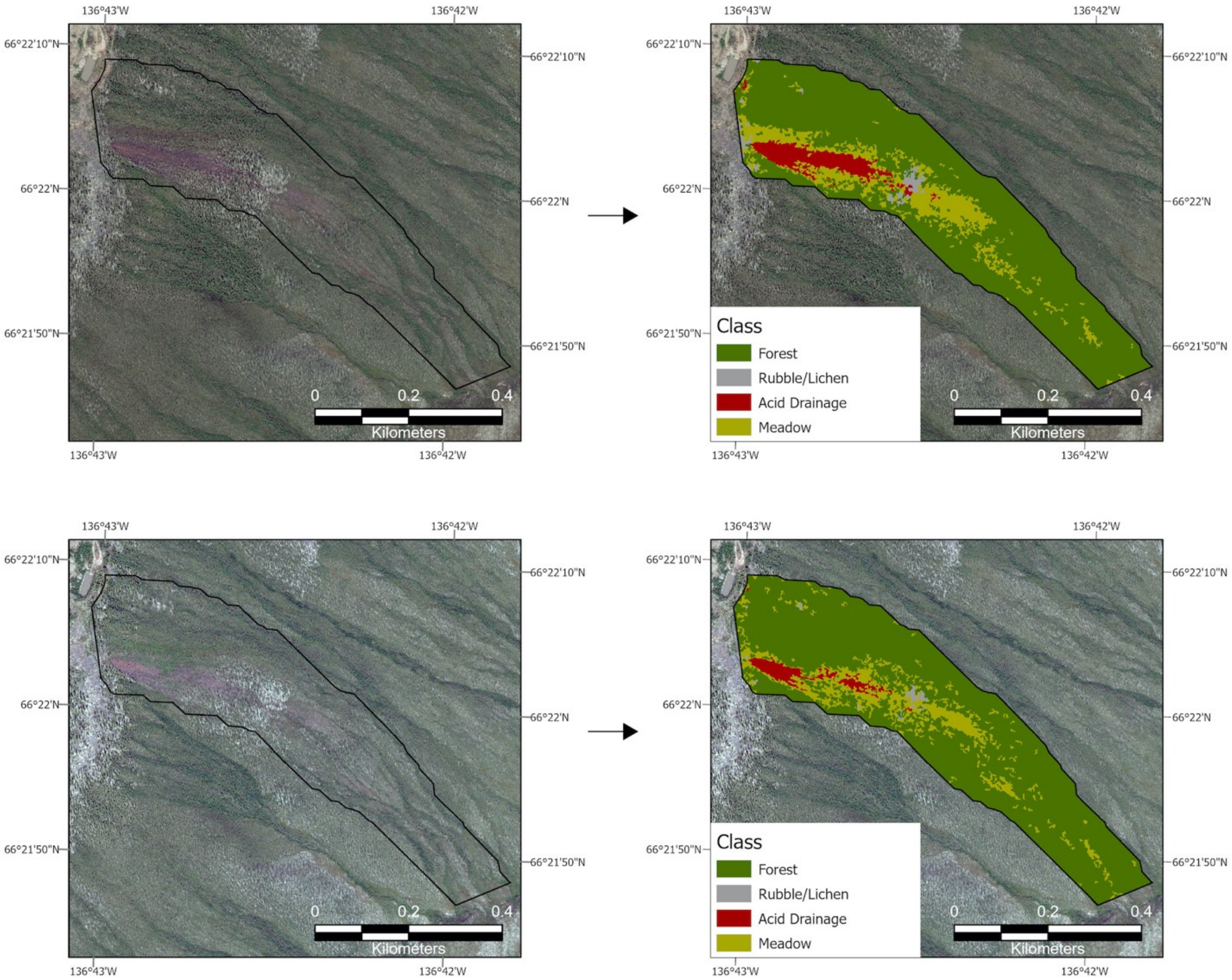

Figure 9. Worldview-2 imagery and post-processed landcover classes at Eagle Plains using supervised classification for (a) June 2014 and (b) July 2021.

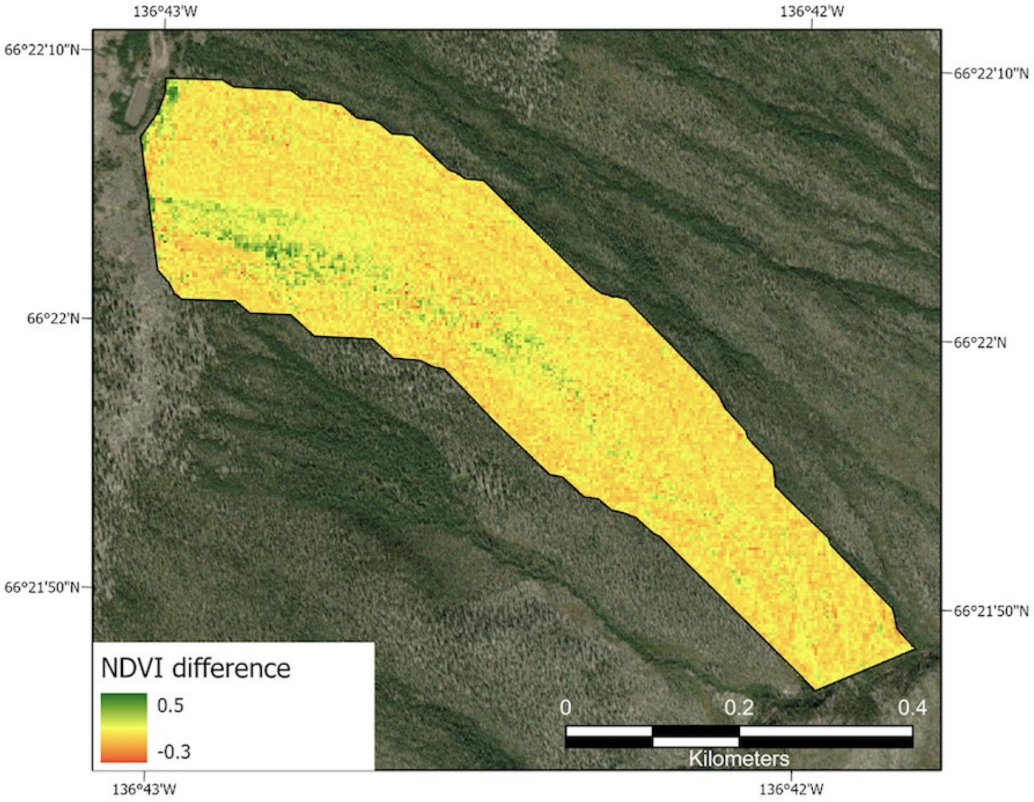

Figure 10. Change in NDVI between June 2014 and July 2021 within the watershed affected by acid drainage. The greening is predominantly occurring within the combined area of the 2014 acid drainage and meadow classes.

5.2 Surface properties and active layer thickness

Near surface sediments in the affected site are a silt loam that increase in silt content downslope (Figure 11a). A similar but more pronounced pattern is found in the adjacent forest, where sandy loam is present near the excavated area which changes to a silt soil downslope. Sediment profiles taken in the affected site show a varying grain size with depth near the excavated area, with a marked increase at 50cm depth (Figure 11b). This coincides with visual observations of a sediment layer heavy with an iron crust. The profile at the site downslope is more uniform and gradually increases in median grain size with depth (Figure 11c).

Visual observations of surface vegetation in the affected site show a gradual increase in vegetation cover downstream of the excavated area, as well as an increase in the types of functional plant types (Figure 13). No vegetation was evident in the first 50m of the transect, but bryophytes, lichens and shrubs started to be found in small amounts until approximately 250m down from the excavated area, when vegetation cover increased to over 40% in the plots surveyed, coinciding with a marked increase in plant functional types. A return to dense and healthy vegetation was found approximately 500m downstream from the excavated area.

Snow depths were recorded during the retrieval of the ground sensors on March 16th, 2022. Snow depths averaged 95 ± 8 cm in the acidic site and 98 ± 7 cm in the adjacent forest. There was no significant difference in snow depth between both sites ($p > 0.05$, 95% confidence).

The thickness of the active layer at the site affected by acid drainage is thicker than in the surrounding non-affected terrain (Figure 12). In the non-affected terrain, the active layer thickness ranges from 31-53 cm (excluding surface rubble at the surface that prevented probing). In the acidic terrain, the active layer ranges from 35 to >100 cm (large rocks prevented probing deeper than 1m). The different active layer thickness between both sites is higher near the excavated area, but progressively diminishes along the transect until 555m, at which point visual evidence of acid drainage was no longer found. The ALT in 2005 was shallower, ranging from 20.5-35 cm in the non-affected terrain and from 27-80cm in the acidic terrain (Figure 12).

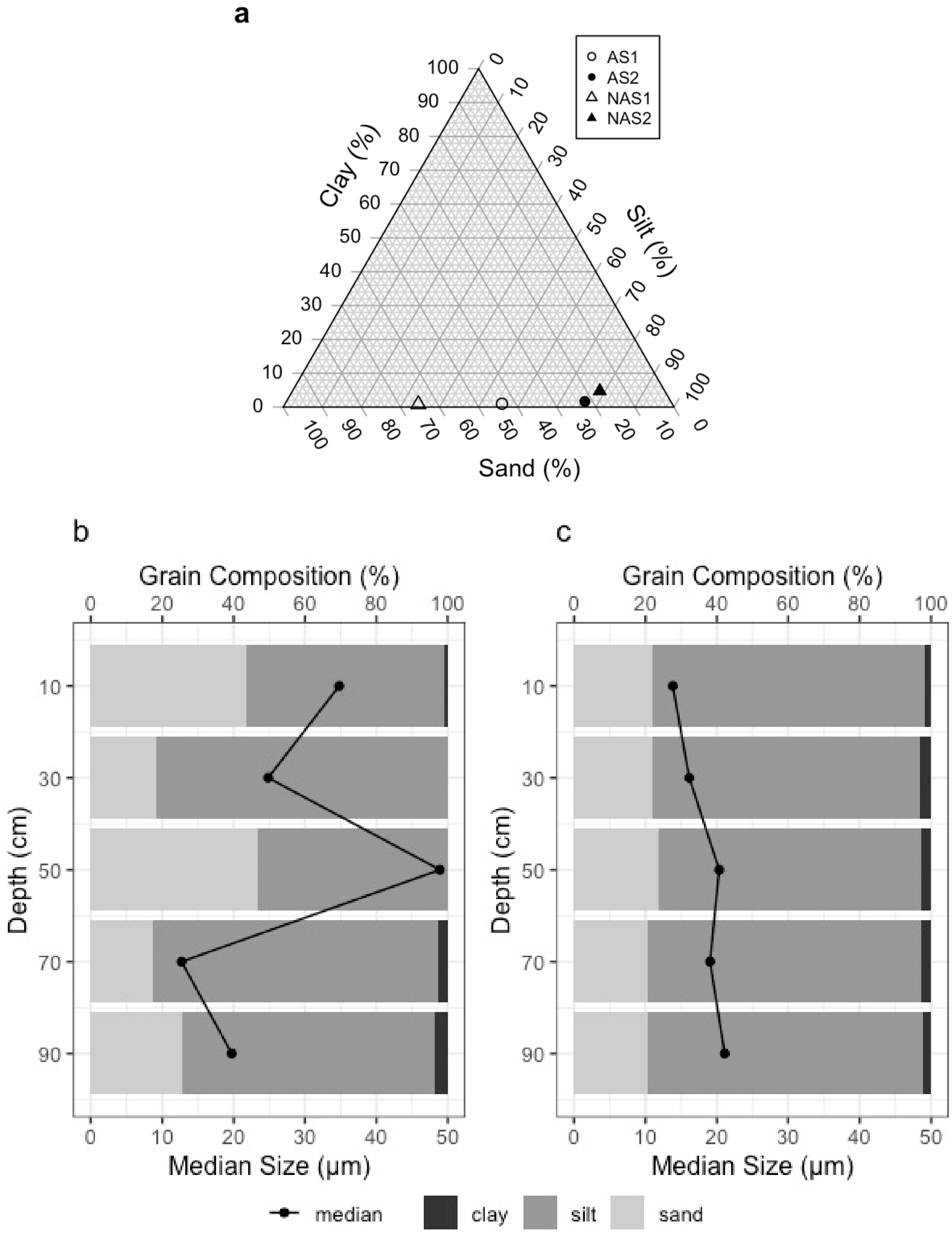

Figure 11. Near surface grain size composition at the top (AS1) and at the bottom (AS2) of the acid drainage site and nearby in the adjacent forest (a). Depth profile grain size composition and median grain size at AS1 (a) and AS2 (b) in the area affected by acid where the Decagon sensors were deployed.

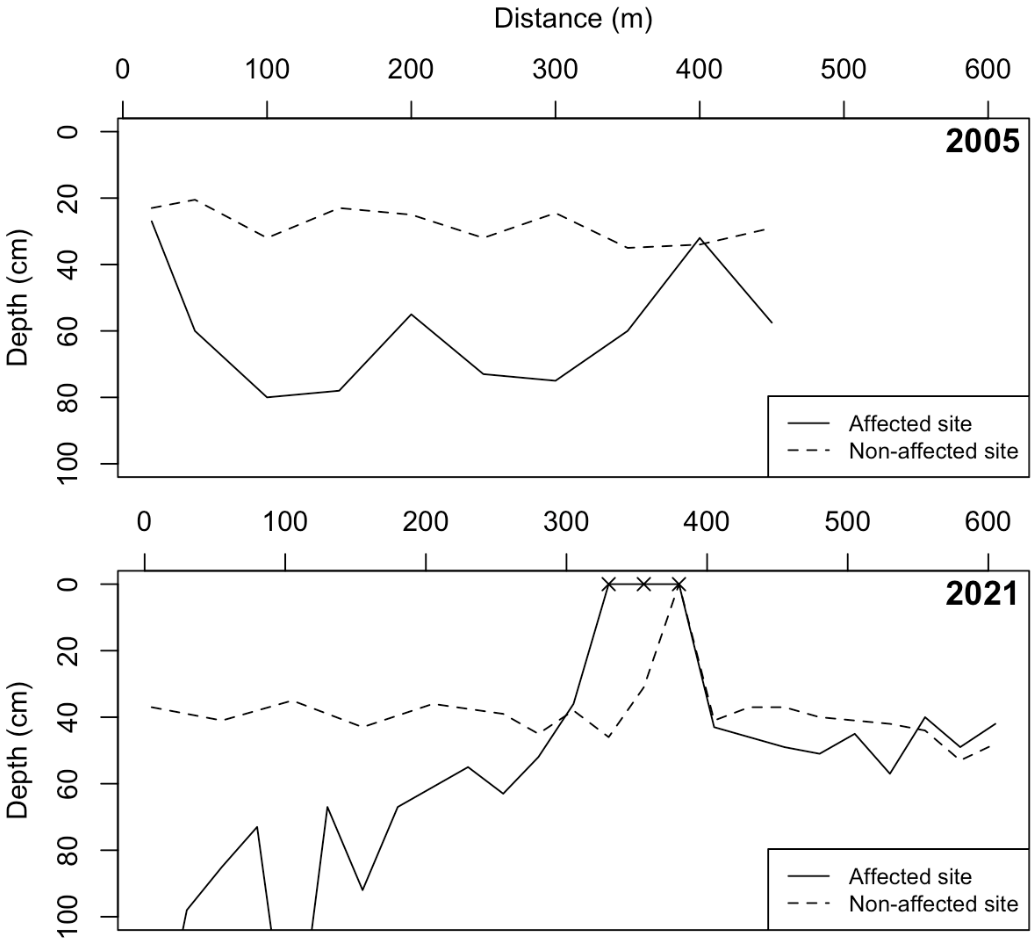

Figure 12. Active layer thickness measured in July 2005 and August 2021 in the area affected by acid drainage and adjacent non-affected forest as a function of distance downstream from the excavated area. Areas where the active layer could not be measured due to surface rubble are indicated with an x. Due to the limited length of the frost probe, values greater than 100 cm could not be measured.

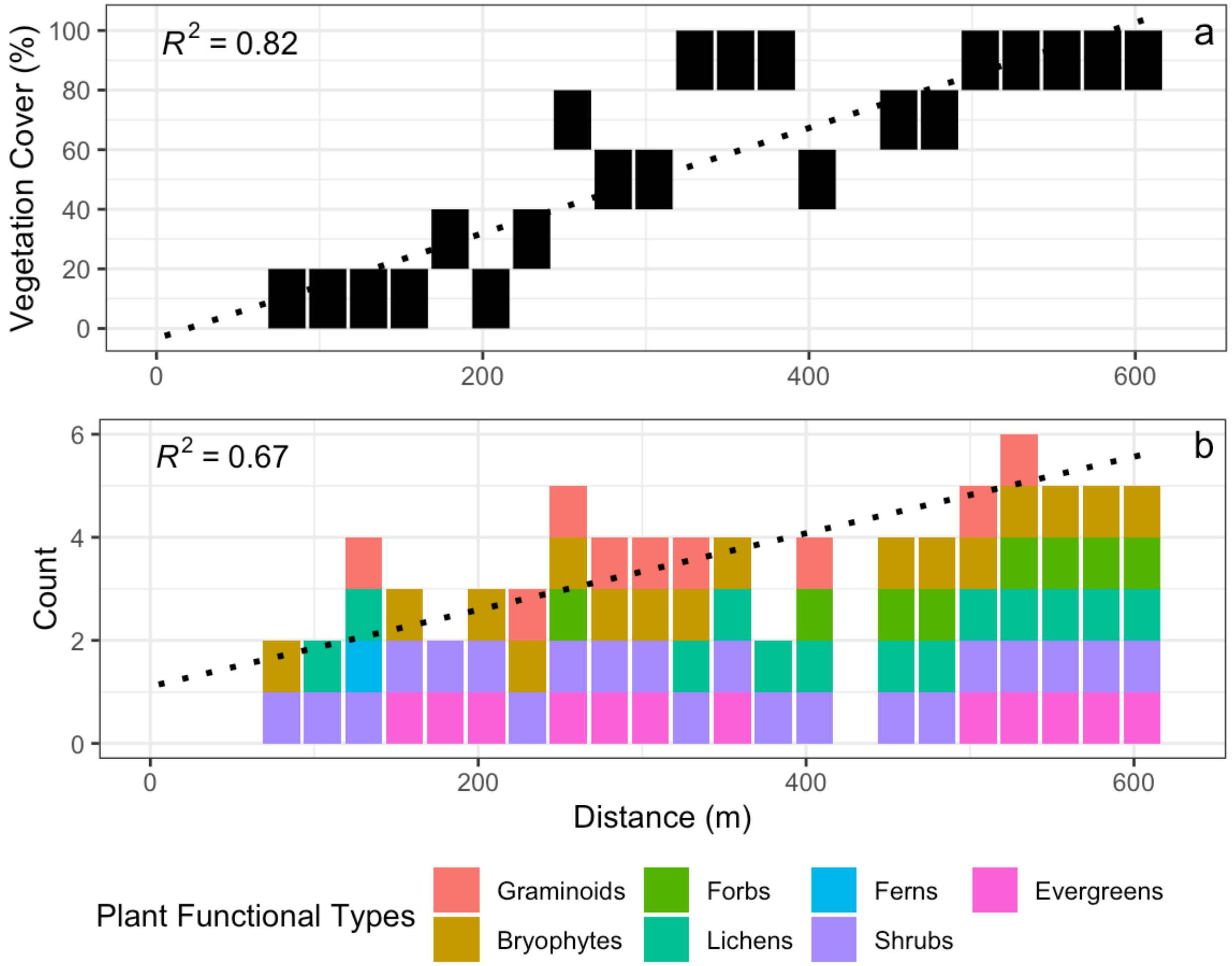

Figure 13. Percent vegetation cover (a) and count of plant functional types (b) at 25m intervals in the acid drainage site.

5.3 Active layer temperatures

Ground temperatures for the affected sites (AS) and the non-affected sites (NAS) from July 2008 to July 2009 are shown in Figure 14. In the NAS, near surface ground temperatures (5cm depth) largely follow seasonal air temperatures and reach a maximum near 10°C, while temperatures at 40 cm depth remains near 0°C during the summer (supporting active layer thickness inferred from probing). In winter, the active layer freezes back and reaches minimum temperatures of -6.8°C and -8.8°C at 40 cm. Near-surface ground temperatures in the acidic zone (5 and 10 cm depth) display warmer temperatures than in the NAS, reaching 20.0°C and 17.3°C respectively. At the AS sites, the active layer only partially refreezes in winter, indicating the presence of a supra-permafrost talik. At both sites, only the near-surface ground temperatures experience values below 0°C (-3.1 to -10.6°C) while temperatures at 60 and 100 cm depth remain near 0°C throughout winter. These different temperature regimes can be seen in Figure 17, which show that sites in the affected area have warmer temperatures during winter and summer with a smaller amplitude with depth compared to non-affected sites. Using historical mean annual air temperatures (MAAT) from the Eagle Plains climate station (1979-2007), the effect of the surface disturbance on ground temperature can be observed in the surface offsets (MAGST – MAAT) where it reaches 8.9°C and 11.1°C at the acid drainage site, whereas it reaches 5.0°C and 5.3°C in the adjacent non-affected terrain. The thermal offsets (TTOP – MAGST) at the affected sites ranges from -3.7°C to -1.7°C while it ranges from -1.0°C to -1.1°C at the non-affected sites.

To further investigate the processes ongoing in the supra-permafrost talik, Decagon 3-in-1 soil sensors were installed in August 2021. Excavations to reach the permafrost table in the acid drainage area were unsuccessful due to the permafrost having degraded beyond a layer of rubble near 80 – 90 cm depth. As such, the soil sensors were installed at 10, 25, 50 and 75 cm depth. The near-surface temperatures indicate partial refreezing of the active layer, with minimum values of -1.7°C (AS1) and -2.1°C (AS2) in mid-March (Figure 15). Ground temperatures at 75 cm depth remained near 0°C throughout winter, decreasing to a minimum of 0.3°C (AS1) and -0.3°C (AS2) by mid-March. Comparing the volumetric water content (VWC) of the soil to temperature, there is a noticeable drop followed by a flattening of the curve in VWC when temperatures drop below 0°C, indicating freezing is taking place (Figure 16). For example, VWC dips < 9% when temperatures decrease below 0°C. At AS1 75 cm depths VWC also decreases as winter progresses but values remain > 10%. As such, freezing might be taking place, but there is still a substantial volume of residual unfrozen water in the supra-permafrost talik.

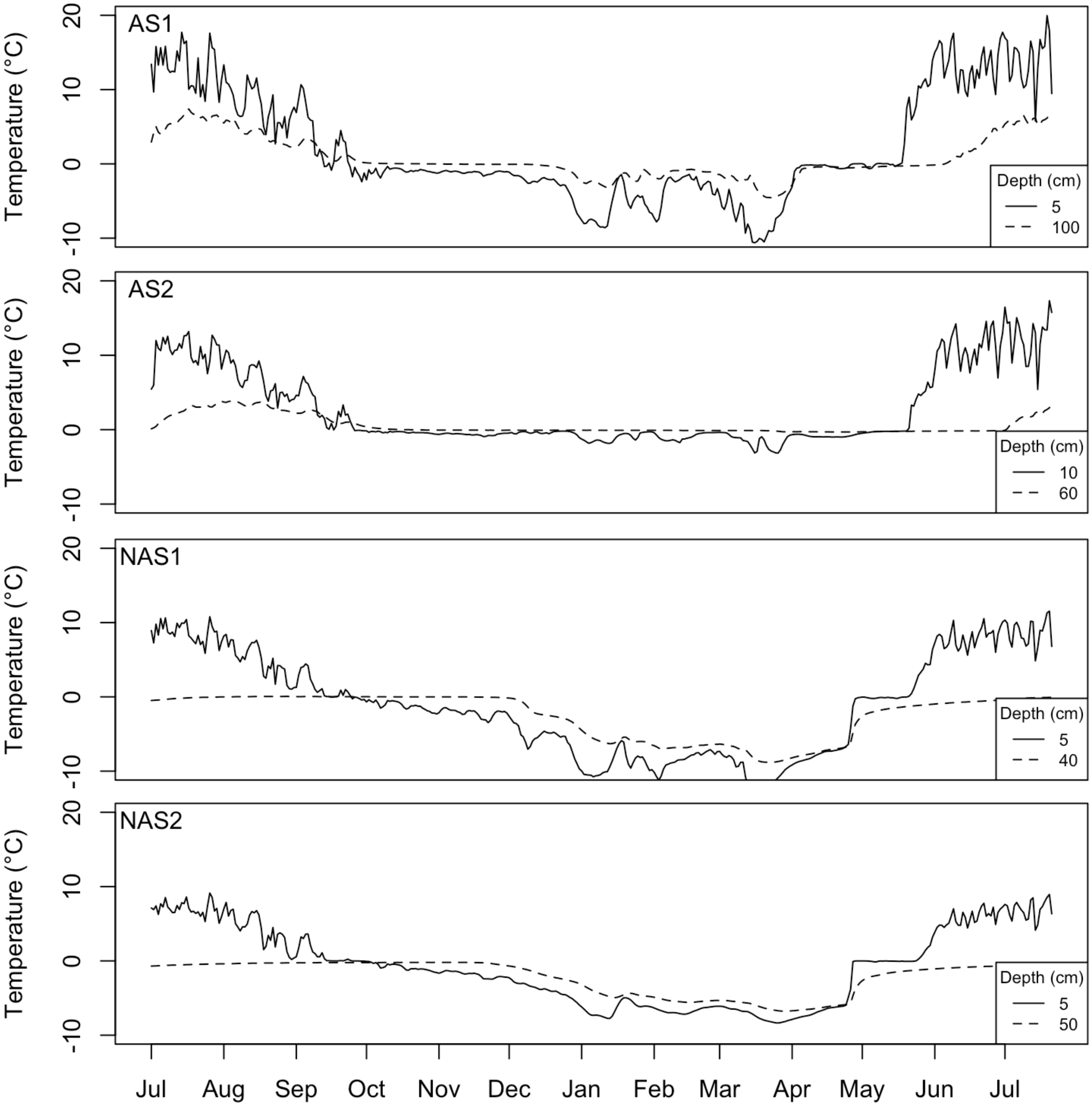

Figure 14. Recorded temperatures at the near surface and at the top of permafrost for the acid site (AS) and non-acid site (NAS) from July 2008 to July 2009.

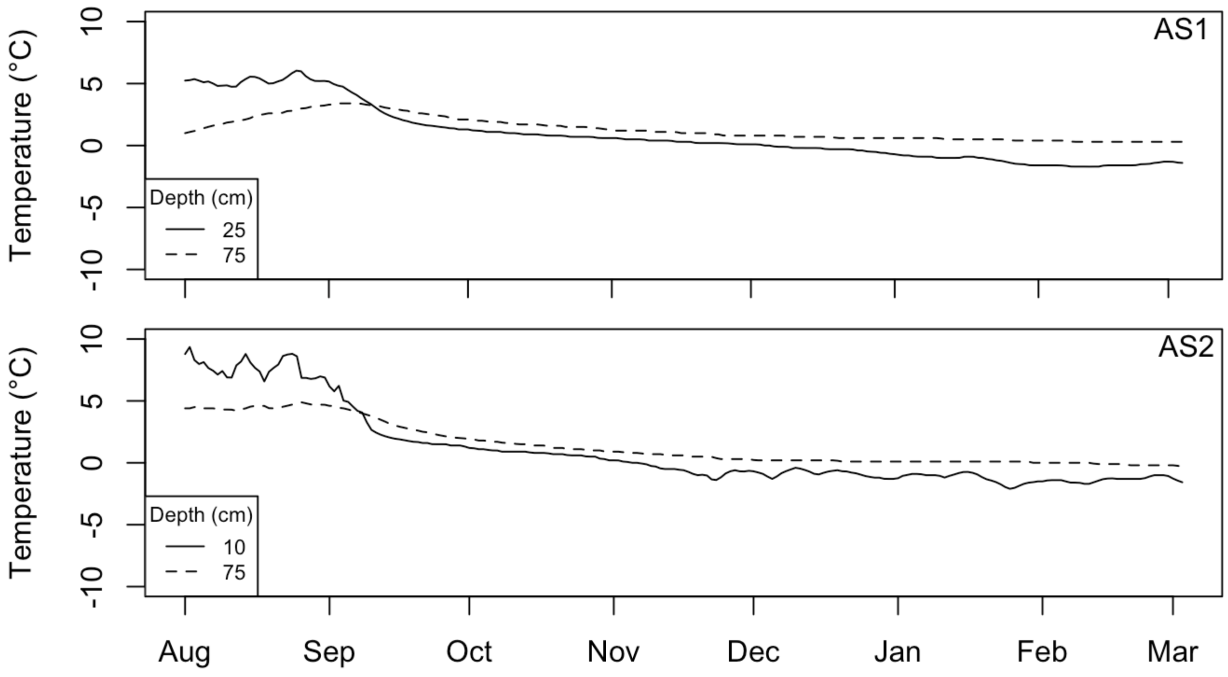

Figure 15. Recorded temperatures in the active layer for the acid site (AS) from August 2021 to March 2022.

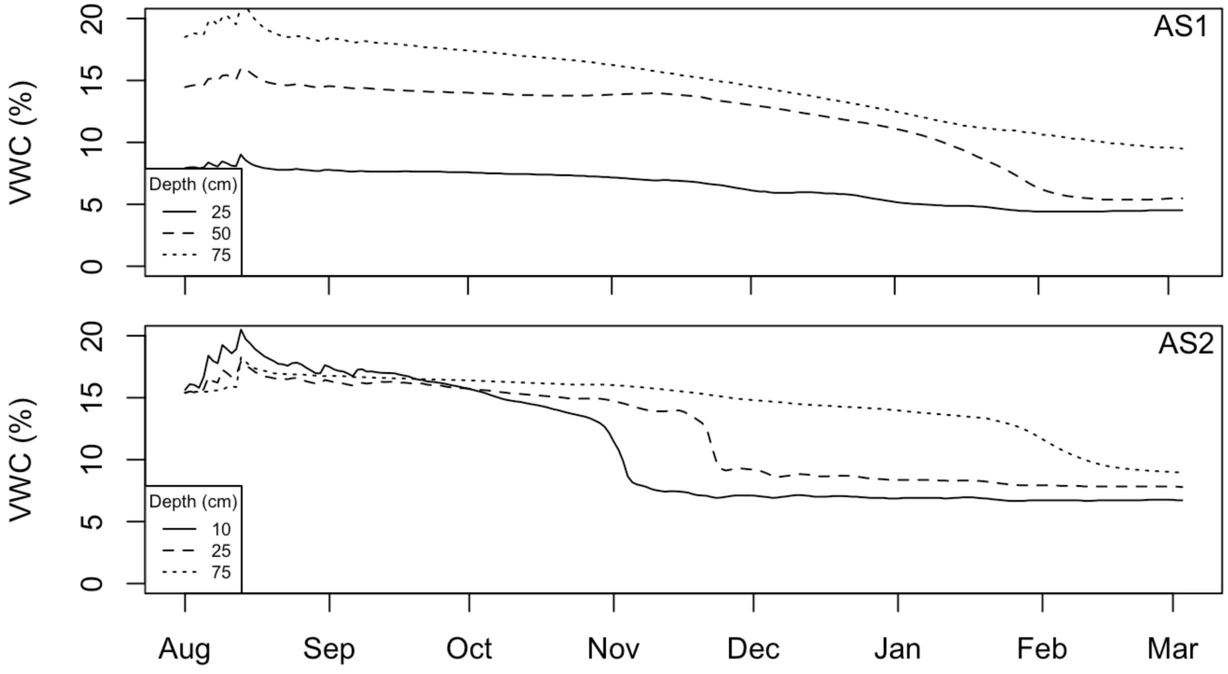

Figure 16. Recorded volumetric water content (VWC) in the active layer for the acid site (AS) from August 2021 to March 2022.

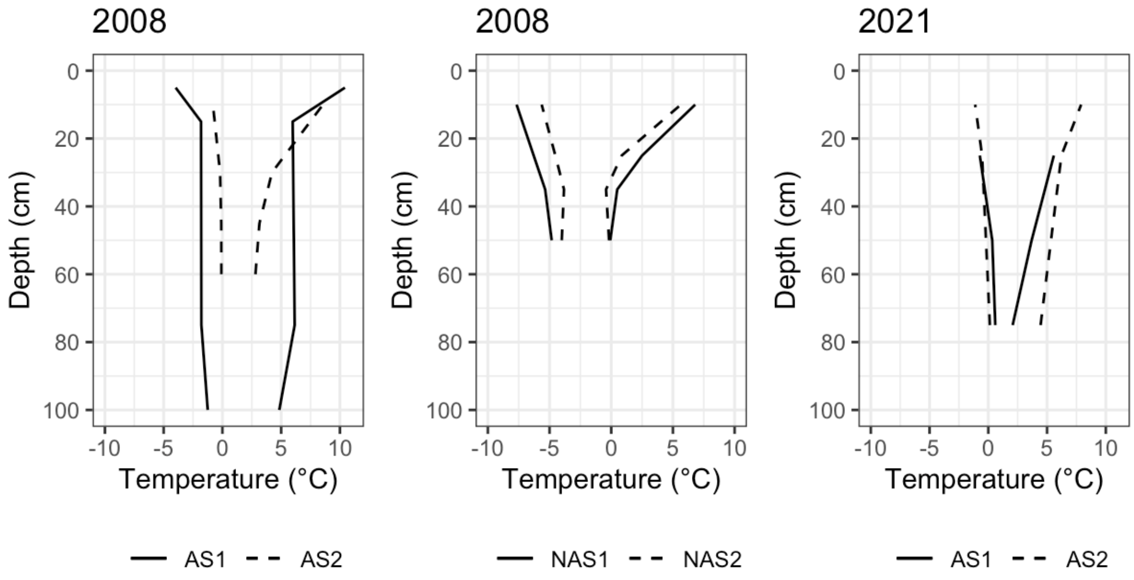

Figure 17. Temperature envelopes for the acid sites (AS) and non-acid sites (NAS) from 2008-2009 and 2021-2022.

5.4 Apparent thermal diffusivity

Temperature sensors installed at different depths in the active layer allowed us to estimate winter and summer apparent thermal diffusivity (D) of the soils in the affected and non-affected sites. Looking at diffusivity values from 2008, sites in the affected area have values 2.7 to 5.1 times greater in the summer and 1.7 to 3.1 times greater in the winter than sites in the non-affected forest (Table 3). Further, seasonal differences in diffusivity are much less important in the affected site. This can be visually observed by comparing the slope of the line of best fit of the time ($\partial T/\partial t$) vs the space ($\partial^2 T/\partial t^2$) derivative, where steeper slopes represent greater D values (Figure 18). These differences are associated in part to changes in surface vegetation between sites, namely the loss of a moss cover which has a low unfrozen conductivity, buffering summer diffusivity values in the unaffected sites. However, the talik found in the affected area is also strongly affecting diffusivity. Since ice has a greater thermal conductivity than water, the diffusivity of frozen ground is greater than for unfrozen ground, leading to the marked seasonal variations found in the unaffected forest. This pattern is not replicated in the affected site, as the ground does not completely freeze through in winter.

Diffusivity values in the affected sites are comparable between 2008 and 2021, except for summer diffusivity at AS1 which is nearly 3 times higher than previously measured (Table 3). Seasonal variations have also become more pronounced (Figure 19). The negative winter slope at AS2 is particularly interesting, and it is accompanied by a negative D_{norm} value. Negative D_{norm} values indicate that non-conductive processes, such as water infiltration, latent heat effects, evaporative cooling and/or vertical water movement are dominant over the conductive tendency as it breaks the assumption of constant heat capacity throughout the soil profile (Outcalt & Hinkel., 1989; Trodahl et al., 2000; Hinkel et al., 2001). Figure 19 should be interpreted knowing this constraint, which highlights the importance of using the geometric diffusivity as it attempts to correct for these errors. However, the magnitude of errors propagates as a function sensor accuracy, which is significantly lower for the Decagon temperature sensors (± 1°C) than for the HOBO sensors used in 2008-2009 (± 0.2°C). As such, recorded differences between both periods could be associated to higher measurement error in 2021. Further, owing to sensor failure at 50 cm depth at AS2, it should be noted that the spatial resolution of our diffusivity measurements is coarser and the depth range for which those values apply larger at AS2 than at AS1 since both are a factor of distance between sensors (Hinkel et al, 2001; Marinova et al., 2022).

Times-series of the space derivative ($\partial^2T/\partial t^2$) further show how the amplitude of temperature variations throughout the active layer is much less important in the affected site compared to the non-affected forest (Figure 20; Figure 21). This shows the effect of higher diffusivity values, which quickly propagate temperature waves and keep ground temperatures from significantly deviating with depth.

Table 3. Mean seasonal D values calculated using normal, inverted and geometric diffusivity functions.

Site	value	Summer (m^2 s^{-1})	Winter (m^2 s^{-1})
AS1 2008	Dnorm	8.05E-07	1.17E-06
	Dinv	8.68E-07	1.17E-06
	Dgeo	8.36E-07	1.17E-06
AS2 2008	Dnorm	3.53E-07	3.89E-07
	Dinv	4.38E-07	5.69E-07
	Dgeo	3.93E-07	4.70E-07
NAS1 2008	Dnorm	1.49E-07	3.60E-07
	Dinv	1.78E-07	4.05E-07
	Dgeo	1.63E-07	3.82E-07
NAS2 2008	Dnorm	1.43E-07	2.63E-07
	Dinv	1.44E-07	2.85E-07
	Dgeo	1.43E-07	2.74E-07
AS1 2021	Dnorm	1.89E-07	7.24E-07
	Dinv	9.14E-05	1.25E-06
	Dgeo	1.31E-06	9.51E-07
AS2 2021	Dnorm	3.07E-07	-1.93E-07
	Dinv	8.20E-07	-1.29E-06
	Dgeo	5.02E-07	4.99E-07

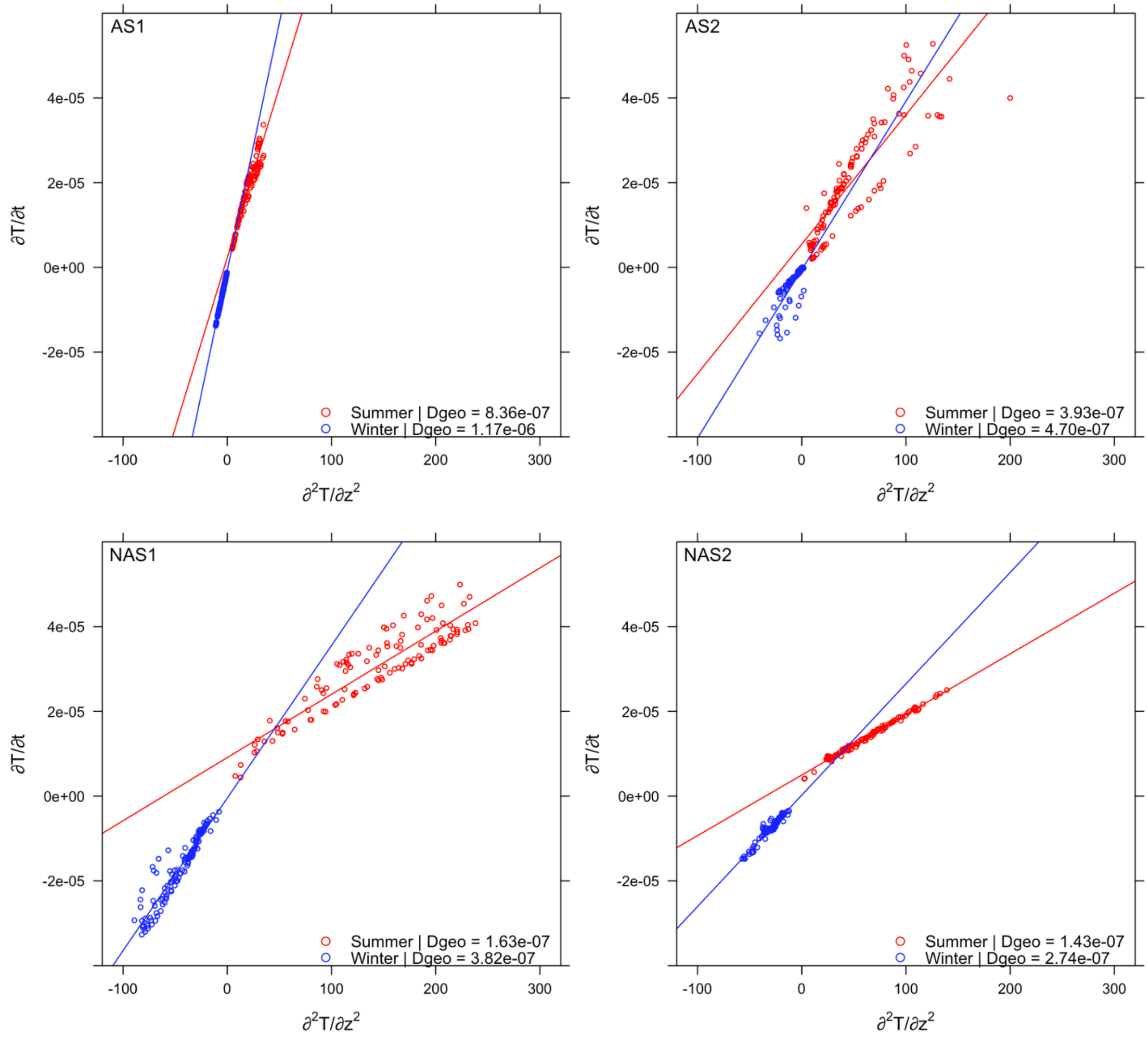

Figure 18. Seasonal apparent thermal diffusivity from July 2008 to July 2009. Winter is considered to last from December to March and Summer from June to August.

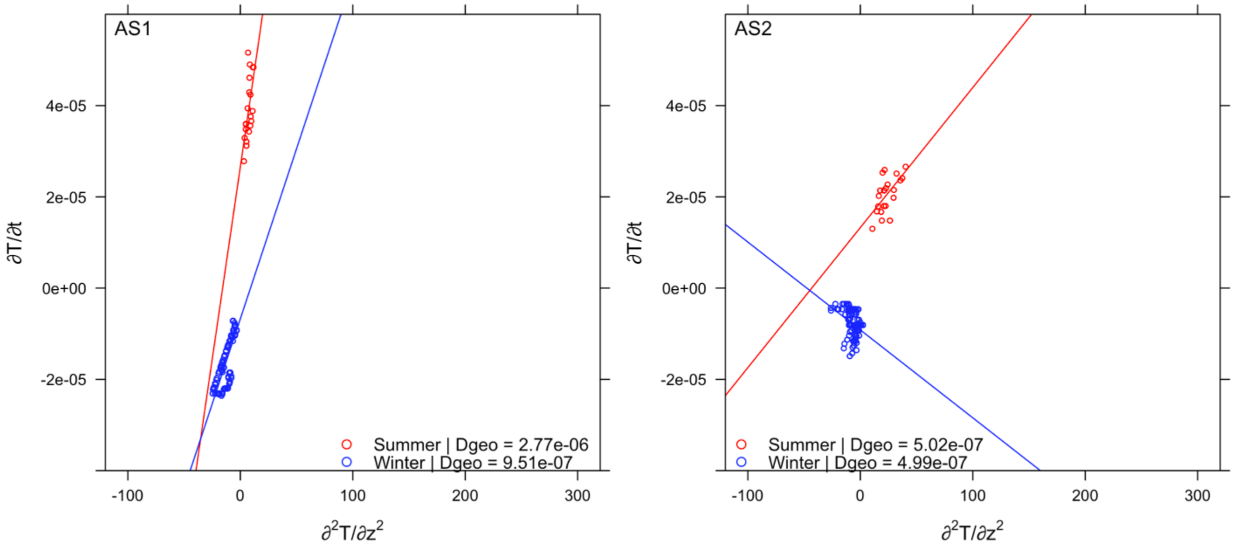

Figure 19. Seasonal apparent thermal diffusivity from August 2021 to March 2022. Winter is considered to last from December to March and summer from June to August.

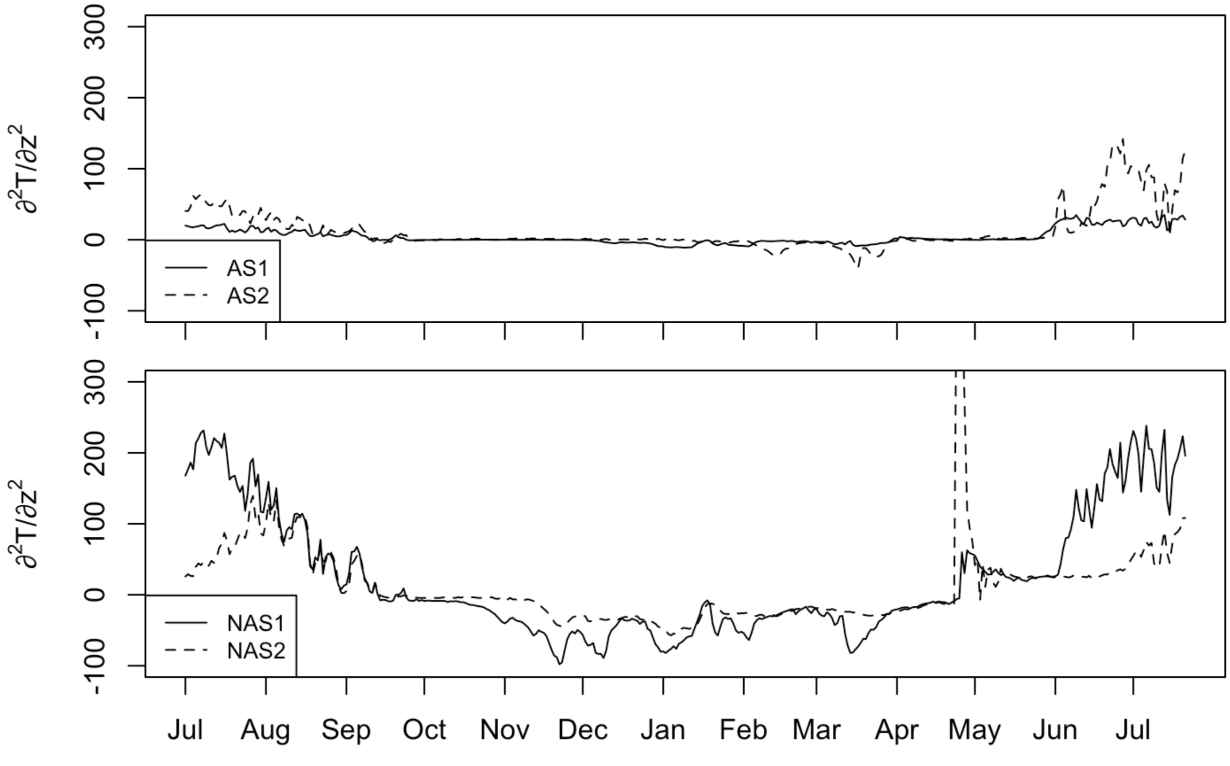

Figure 20. Second order derivative ($\partial^2T/\partial z^2$) of the active layer thermal profile showing normalized differences in temperature throughout the active layer from 2008-2009.

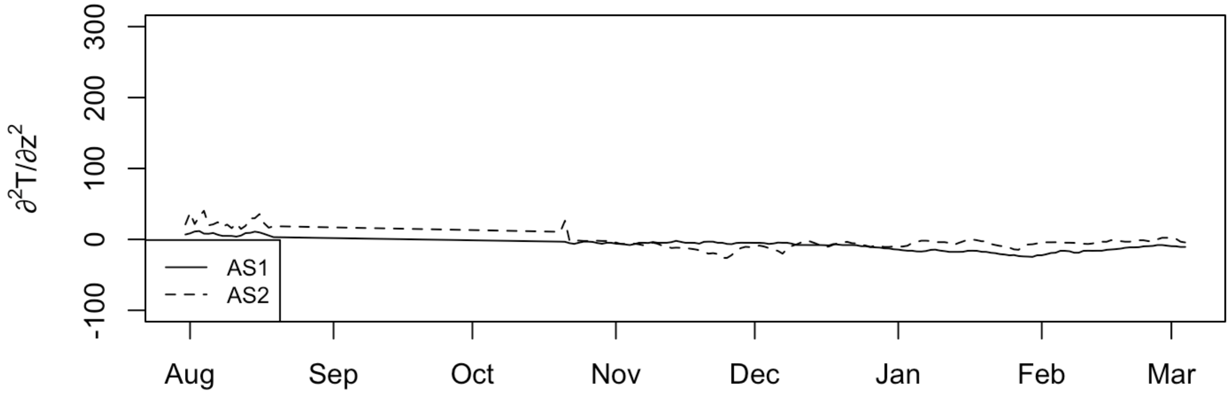

Figure 21. Second order derivative ($\partial^2T/\partial z^2$) of the active layer thermal profile showing normalized differences in temperature throughout the active layer from 2021-2022.

5.5 Active layer geochemistry

The soluble active layer solute concentrations in the acidic site are dominated by SO_4 (1362.8 ± 647.7 mg/L), Ca (124.6 ± 121.0 mg/L) and Fe (26.7 ± 29.1 mg/L), while containing trace amounts of Al (17.8 ± 10.5 mg/L), Mg (14.9 ± 10.4), Na (011.5 ± 5.5), Zn (1.4 ± 0.7 mg/L) and Cl (4.4 ± 5.4) (Figure 22; Table 5 – Appendix 1;Table 6- Appendix 1). Total dissolved solids average 1568.4 mg/L with a charge balance error of 5% and an average pH of 3.2 ± 0.6. Cl, Fe and SO_4 concentrations are several times higher at the site near the excavation than the downstream site, while Ca, Mg, Mn and Zn are higher at the downstream site. Solute concentrations throughout the depth profile are variable, however they peaked twice where the soil layer was thick with Fe hydroxide near 35cm and 50cm at AS1 and once near 50cm at AS2. pH values sharply decrease from the surface at both sites, however the pH at AS2 increases significantly between 50 and 75 cm in depth before returning to lower values. Sites in the surrounding forest have acidity values two order of magnitude lower than in the area affected by acid drainage, with an average pH value of 4.9 ± 0.418. 80. Solute levels are significantly lower with a TDS averaging 256.6 mg/L dominated by SO_4 (93.1 ± 59.8 mg/L), K (33.5 ± 18,3 mg/L), Ca (33.4± 23.3 mg/L), Fe (30.1 ± 32.5 mg/L) and Na (25.7 ± 12.2 mg/L) (Table 7- Appendix 2). Ions tend to increase in depth, save for K, Cl and Na and Fe (top site).

The freezing point depression caused by active layer solutes was calculated from the formula:

$$T_f = K_f \times m \qquad \text{(Eq. 12)}$$

Where T_f is the freezing point depression, K_f is the freezing point depression constant and m is the molality. The freezing point depression is one order of magnitude higher the acidic site (0.034-0.039°C) than in the surrounding forest (0.007-0.013°C). These values are slightly lower than what was found in the acidic site in 2005 (0.05-0.1°C).

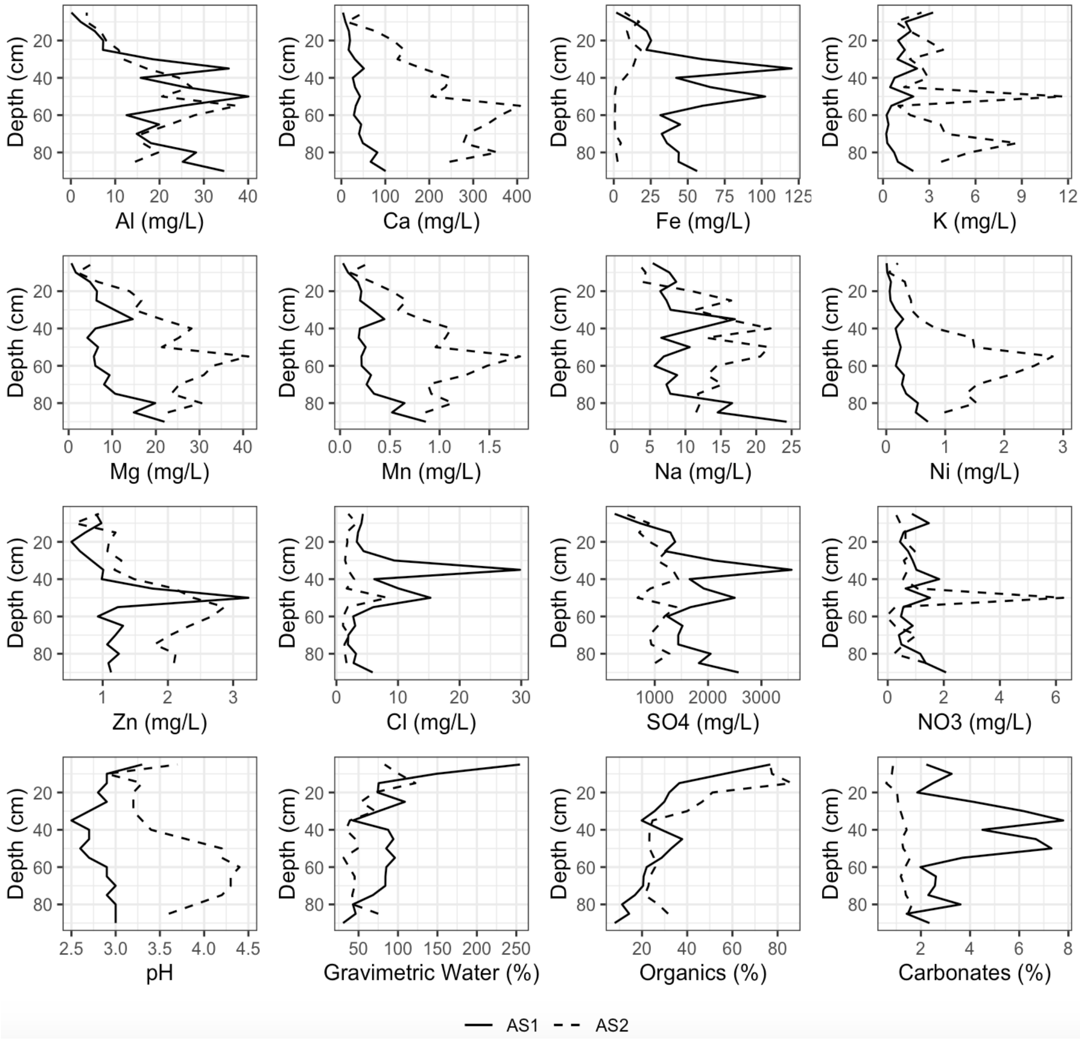

Figure 22. Active layer geochemical profiles at AS1 and AS2.

6. Discussion

6.1 Permafrost conditions

Results from our field investigations indicate that permafrost degradation has been ongoing at the site since 2005 (Lacelle et al., 2007, Figure 12). The active layer thickness in both the affected site (73 ± 20 cm) and the non-affected forest (39 ± 11 cm) have increased, and this may be due to an increase in mean temperature associated with climate change (Lantz & Kokelj, 2008; Jorgensen et al., 2010). Nonetheless, the degradation occurring in the acidic site has been more important than in the forest, and the permafrost table was not reached while digging pits at both AS1 and AS2.

While it was initially believed that differences in snow depths between the affected site and the adjacent forest was a cause for permafrost degradation, field investigations showed it was not the case. The snowpack in March 2021 was relatively high (96 ± 8 cm) and it was observed that the spruce trees in the surrounding forest have too small a canopy to significantly intercept snow. It is associated at least in part with the loss of vegetation at the site which has changed the energy balance at the ground surface by 4 to 6°C compared to the forested sites, however it is unknown whether the exothermic reaction occurring from the microbial oxidation of sulfide contributes to the degradation.

The effect of the change in energy balance can be investigated by modelling the active layer thickness using the Stefan formula which provides a simple yet commonly used formula to estimate the depth of thaw:

$$z_t = \sqrt{\frac{2k_t s DDT_a}{\rho w L}} \qquad \text{(Eq. 13)}$$

Where z_t is the active layer thickness (m), k_t the thermal conductivity of the thawed soil (W m^{-1} °C^{-1}), s a scaling factor (s d^{-1}), DDT_a the air temperature thawing degree days (°C days), ρ the soil density (kg m^{-3}), w the soil moisture ratio by weight (dimensionless) and L the latent heat of fusion (J Kg^{-1}). Soil density (kg m-3) and heat capacity (J Kg^{-1} °C^{-1}) values were obtained from Shiklomanov & Nelson (1999) and used to solve for k knowing seasonal diffusivity values. The formula assumes that the only form of heat transfer in the soil is from latent heat due to phase change, and neglects volumetric heat transfer (Andersland and Ladanayi, 1994). To account for the sensors being buried 5 cm into the active layer, DDT_a can be estimated from temperature measurements at depth using a sub-surface n-factor, n_{dt}. It is calculated using the formula from Riseborough (2003) which considers the change in temperature to a be function of the squared difference between the surface and the relative depth of the sensor in the active layer:

$$n_{dt} = \left(1 - \frac{d}{z}\right)^2 \qquad \text{(Eq. 14)}$$

where d is the depth of the sensor and z is the active layer thickness. DDt_a can then be calculated as:

$$DDT_a = \frac{DDT_d}{n_{dt}} \qquad \text{(Eq. 15)}$$

This gives us an ALT of 36 cm in the forest and of 83 cm at the acidic site, well within the bounds of recorded ALT at both sites (Figure 23). This demonstrates that the exothermic oxidation of sulfide by soil microbes does not significantly contribute to permafrost degradation as changes in thermal conductivity and soil moisture content from the loss of surface vegetation explain the difference in the ALT. This finding is consistent with studies detailing an increase in ALT following wildfires due to the loss of vegetation increasing ground surface temperatures and an increase in soil moisture content from reduced evapotranspiration (Smith et al., 2015; Holloway & Lewkowicz, 2020)

Recorded near surface temperatures were much more variable in 2008 than in 2021, indicating that the insulating layer of snow was likely comparatively thin. Though it falls within the bounds of recorded variability from 1981-2007 (79 ± 30 cm), the snowpack in 2021 was high enough to significantly buffer the ground from air temperatures, potentially being a reason why isothermal conditions remain at depth. To estimate the influence of the snowpack on the freeze-back of the active layer, the Stefan equation can once again be used to model downward freezing by replacing thawing indices with freezing indices and adding a scaling *n-factor* (n) to account for the insulating effect of snow on ground temperatures, such that:

$$z_f = \sqrt{\frac{2k_f s(n)DDF_a}{\rho w L}} \qquad \text{(Eq.16)}$$

The scaling n-factor (n) is calculated as the ratio of DDF measured from air temperatures (DDF_a) to DDF measured at the ground surface (DDF_s):

$$n = \frac{DDF_a}{DDF_s} \qquad \text{(Eq.17)}$$

Using the range of possible n-factors from 1 to 0.01 and keeping DDF_a constant, we see that the talik at the acidic site requires little snow accumulation to persist (Figure 24). Under an n-factor of 0.5, which for areas having a MAAT of -6°C equals a snowpack greater than 20 cm (Smith & Riseborough, 2002), the freezing front cannot penetrate to the shallowest depth of measured ALT in the first 100 m of the acidic site, the area where the reaction is most important. A snowpack of this size or smaller has never occurred in the climate record from 1979-2008 (min = 31 cm). Further, the temperature at the top of permafrost at the site is warm (~0°C) and significantly higher than in the forest (Figure 17), indicating that upwards freezing is likely not contributing much to the freezing of the active layer. From this we can conclude that the talik remains from year to year even with variable snowpack depths, and that the presence of the talik is predominantly due to the ALT being too thick to completely freeze back in winter.

In contrast, the modeled freeze-back of the active layer in the forest is more sensitive to snow depths owing to the lower thermal conductivity at the site. It's only under an n-factor of 0.5 that the active layer completely freezes over, indicating that a talik may potentially occur in the forest when snow accumulation is high. However, it is important to keep in mind that the snowpack accumulates over several months throughout winter, and complete downward freezing can occur before the critical threshold of snow accumulation is reached. This also doesn't account for upward freezing from the top of permafrost, which would be much more important in the forest than in the acidic site given the significantly lower permafrost temperature (Figure 17). Nonetheless, it may be that consecutive years of early and heavy snow accumulation may result in an increase in the ALT in the forest due to incomplete freeze-back in winter. While the climatic records at Eagle Plains ended in 2008, the trend for the maximum annual snow accumulation for the period of available data from 1979-2007 was increasing, as was the trend for mean annual temperature (Figure 25). If these trends continued into the following decade, it may explain the increase in the ALT in the forest between 2005 and 2021 and would also account for a part of the increase at the acidic site. This aligns with recent reports describing an increase in talik development throughout a range of conditions in Alaska partly due to a decrease in FDD and an increase in snow depths (Farquharson et al., 2022).

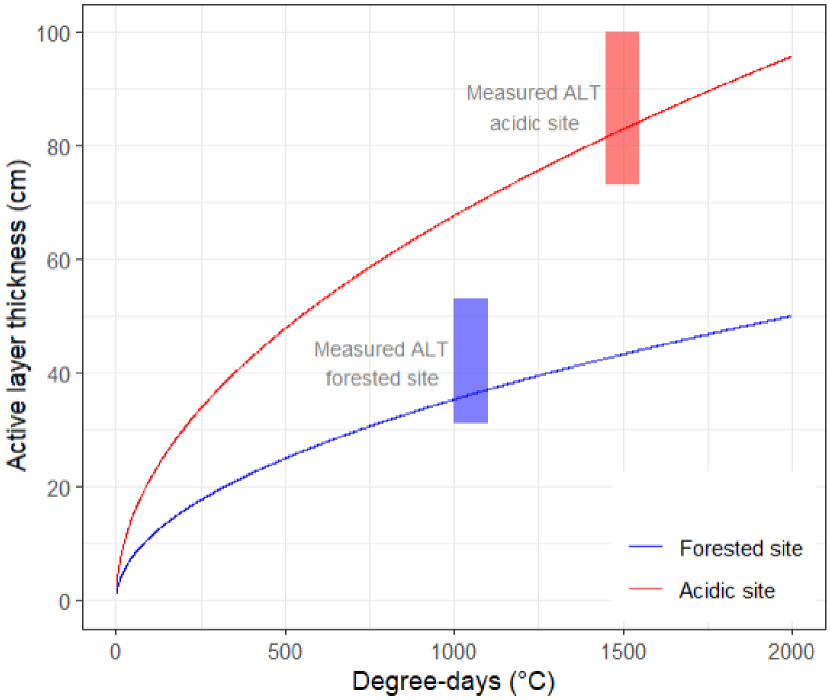

Figure 23. Modelled active layer thickness at both the forested and acidic site using the Stefan formula.

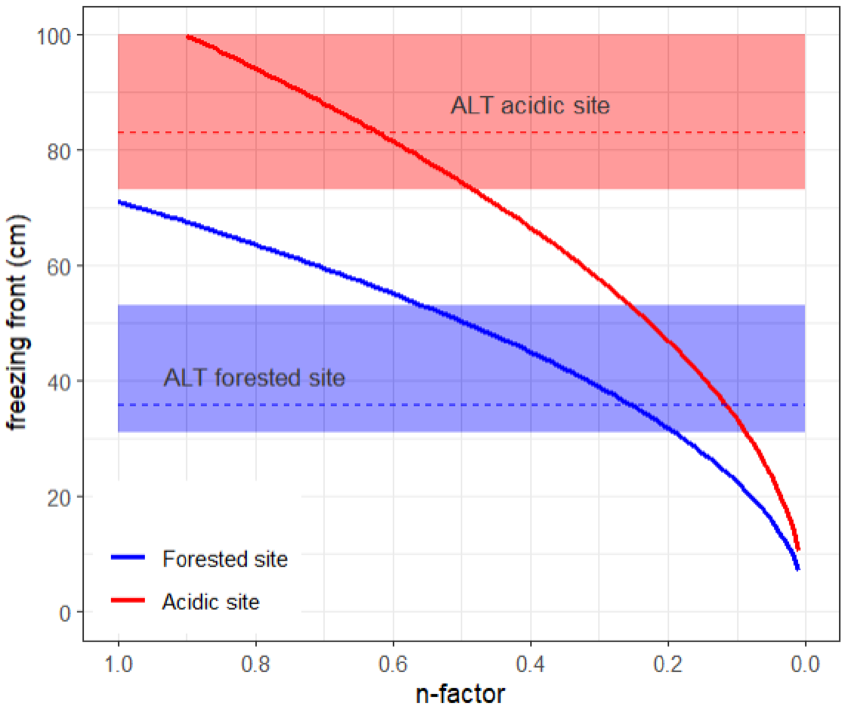

Figure 24. Freezing front penetration as a function of n-factors keeping DDF_a constant. Boxes represent measured ALT and dashed lines modelled ALT for depth of thaw.

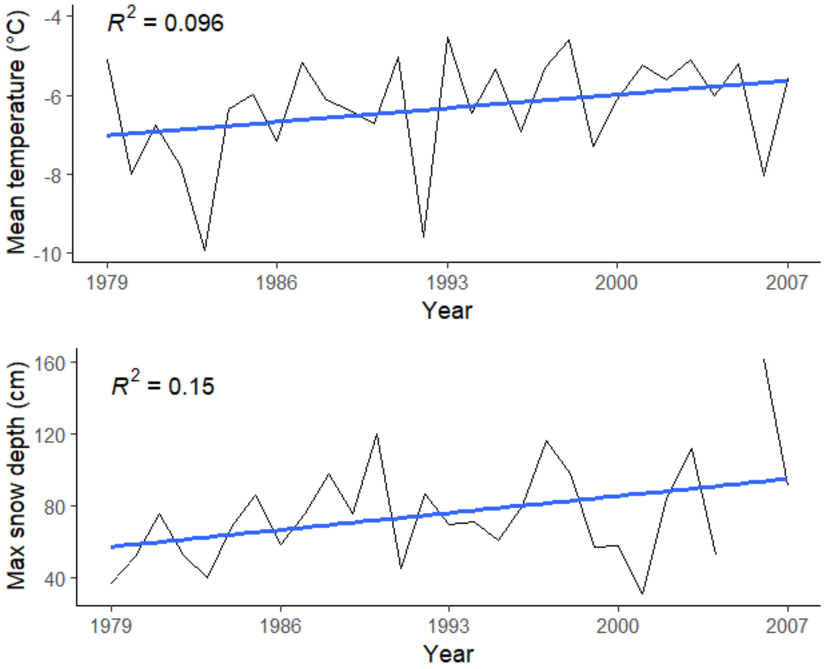

Figure 25. Mean annual temperature and maximum recorded snow depth at Eagle Plains climate station from 1979 to 2007. Snow data unavailable for 2005.

Table 4. Input parameters used to calculate active layer thawing and freezing depths using the Stefan equation.

Parameter	AS	NAS	units
$\boldsymbol{k_t}$	0.87	0.17	W m^{-1} °C^{-1}
$\boldsymbol{k_f}$	1.2	0.4	W m^{-1} °C^{-1}
$\boldsymbol{s}$	86 000	86 000	s d^{-1}
$\boldsymbol{DDT_a}$	1500	1045	°C days
$\boldsymbol{DDF_a}$	3436	3436	°C days
$\boldsymbol{\rho}$*	1396	1396	kg m^{-3}
$\boldsymbol{w}$	0.7	0.5	dimensionless
$\boldsymbol{L}$	334 000	334 000	J Kg^{-1}
$\boldsymbol{C_p}$*	745	745	J Kg^{-1} °C^{-1}

* values taken from Shiklomanov & Nelson (1999)

6.2 Insights using apparent thermal diffusivity

Differences in diffusivity found between the area affected by acid drainage and the non-affected forest highlight the strong effect the loss of vegetation has on the thermal profile of the soil (Figure 18; Table 3). The combined effects of the loss of surface organics and the presence of a supra-permafrost talik result in soils with higher diffusivity and little seasonal change. This amplifies the thermal effect of increased insolation from the loss of vegetation on summer ground temperatures as more energy is transferred at depth, resulting in more permafrost thaw. Higher permafrost temperatures (Figure 17) further limit upwards freezing from the top of permafrost in winter and reduces the quantity of energy required to thaw the active layer in the spring. This induces a positive feedback loop that degrades the underlying permafrost until equilibrium is again reached.

6.3 Vegetation recovery from acid drainage caused deterioration

Two key questions asked as part of this work is whether (1) the rate of sulfide oxidation is as high as in 2008 at the site, and (2) is the size of the affected area growing or shrinking? Although surface waters were not present at the time of our return to the site in 2021, preventing us from making a direct comparison of sulfide oxidation rates made during earlier investigations, active layer concentrations of SO_4 are comparable to values in 2005 and 13 to 30 times higher in the affected site compared to the non-affected forest, while pH concentrations are nearly 3 orders of magnitude higher at the top of the site and 1 order of magnitude higher at the bottom of the site than in the surrounding forest (Table 5-7 – Appendix 1). These values, along with the lack of vegetation and the presence of ferrihydrite near the stream outlet (Figure 26a), suggest that oxidation of the shale bedrock is ongoing, and that acidic water is still discharging.

Nonetheless, the site seems to be recovering from the effects of acid drainage reported in Lacelle et al. (2007), and our results show a 53% decrease in acid drainage classified area between 2014 and 2021 (Table 1; Figure 9), accompanied with a greening trend within the acid drainage and meadow boundaries assessed in 2014 (Figure 10). Further, while a direct comparison of our results is difficult given different sampling points, our results indicate a significant increase in vegetation cover downslope from the stream outlet (Figure 13a), which was not seen in earlier investigations where vegetation cover remained extremely low near the stream (Lacelle et al. 2007). A significant increase in plant functional types is also seen downstream from the outlet (Figure 13b), and spruce sapling recruitment was observed to be occurring as close as 155m from the stream outlet and increasing downslope (Figure 26b). While more intensive categorization of plant functional types has been used to determine ecological degradation and restoration (Gondard et al. 2003), our results nonetheless indicate that the local flora is rebounding from past deterioration considering the site was principally covered by forest in the past.

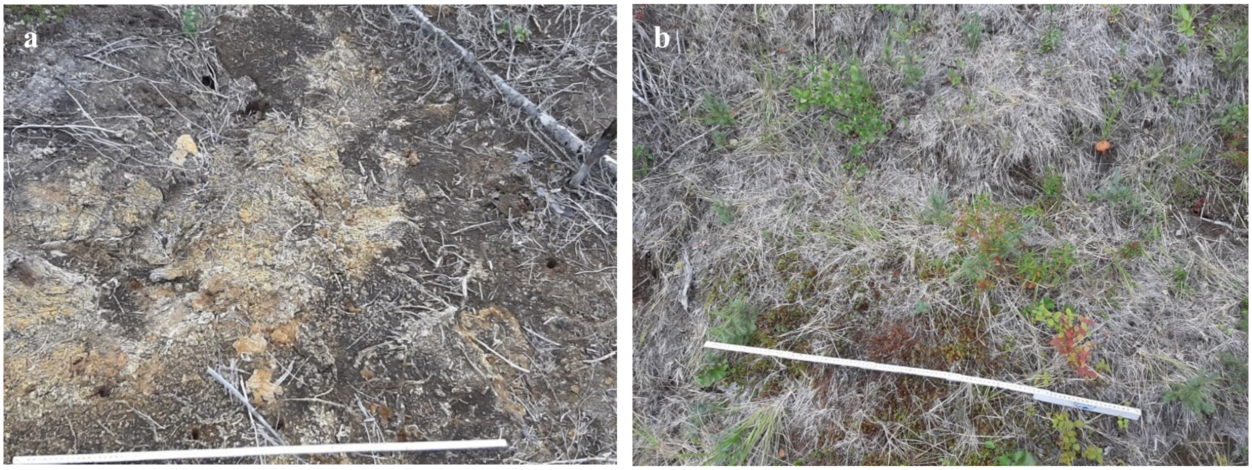

Figure 26. Ferrihydrite is still found to occur in within 100m of the stream outlet in the affected area (a). Spruce sapling recruitment is high 280m downslope from the stream outlet (b).

Although a reduction in the rate of pyrite oxidation cannot be used to explain the recovery of vegetation at the site, evidence suggests it may be related to the increase in active layer thickness observed at the site since 2005. If ground ice concentrations are low and soil drainage possible, an increase in permafrost depth can result in greater infiltration and lower water tables (Jorgensen et al., 2013). Considering the surface conditions and slope found at the site, this seems to be the case at Eagle Plains. This change in the hydrological conditions, along with the intermittent nature of the acidic stream discharge, should result in greater infiltration of stream waters into the active layer, leading to increased groundwater flow, less surface water flow and greater dissemination of soluble ions into the increasing volume of active layer sediment. This would explain why soluble ion concentrations remain high near the stream outlet (TDS = 1818.4 mg/L) but are lower downslope (TDS = 1304.4 mg/L), especially in relation to products of sulfide oxidation SO_4 (1686.2 mg/L down to 1020.4 mg/L) and Fe_{tot} (45.7 mg/L down to 6.5 mg/L). This gradient was not observed in 2005. Seepage of surface contaminants and acidity at greater depths with meteoric water and snowmelt would also occur during the summer, which would be further reinforced by the exclusion of solutes ahead of the freezing front during the freeze-back of the active layer in winter, creating more viable conditions for plant establishment at the surface. As such, permafrost degradation has allowed surface conditions to become more favorable to the colonisation of plants. Given sufficient time, it would be expected that this return to favorable ecological conditions for plant life would act as a negative feedback to permafrost degradation as the surface organic mat returns and soils become buffered from warm summer temperatures (Jorgensen et al., 2010; Smith et al., 2015; Holloway & Lewkowicz, 2020).

7. Conclusions and future work

This research aimed to investigate the effects of acid drainage on active layer thermal properties and surface expression. Analyzing field data and satellite imagery, we have determined that:

1. Permafrost degradation associated with acid drainage is due to the loss of vegetation increasing ground surface and active layer temperatures by 4°C to 6°C, which also increases the thermal diffusivity of the soil as the buffering effect of the surface organic mat is reduced;
2. The diffusivity of the active layer shows little seasonal variation in acid drainage affected soils as the larger ALT prevents a complete freeze-back of the active layer and maintains a supra-permafrost talik.
3. The combination of higher summer diffusivity and higher permafrost temperatures reducing upward freezing act as a positive feedback to ongoing permafrost degradation until equilibrium is reached;

4. The surface expression of acid drainage at Eagle Plains has decreased by 53% from 2014 to 2021 and is being replaced by successional changes in vegetation as meadow plants recolonize the surface;
5. Improved drainage due to thawing permafrost can be conducive to plant establishment even though acidic water discharge is ongoing, which may potentially act as a negative feedback to permafrost degradation given long time scales.

While we have determined how permafrost degradation occurs following initiation of acid drainage, further work still lies to investigate if an increase in unfrozen water content due to high soluble ion concentrations leads to more ground ice accretion at the top of permafrost. Should it occur, it would act as an important negative feedback to permafrost degradation and be an important factor to consider when planning remediation operations and permafrost modelling.

References

Almeida, Schaefer, C. E. G. R., Fernandes, R. B. A., Pereira, T. T. C., Nieuwendam, A., & Pereira, A. B. (2014). Active layer thermal regime at different vegetation covers at Lions Rump, King George Island, Maritime Antarctica. Geomorphology (Amsterdam, Netherlands), 225, 36–46.

Amiro, B. D. (2001). Paired-tower measurements of carbon and energy fluxes following disturbance in the boreal forest. Global Change Biology, 7(3), 253-268.

Andersland, O. B., & Ladanyi, B. (1994). *An introduction to frozen ground engineering*. Chapman & Hall.

Anderson, D., Tice, A., McKim, H. (1973) The unfrozen water and apparent specific heat capacity of frozen soils. Permafrost Second International Conference. Washington, DC. National Academy of Science, 289-295.

Anderson, S., Drever, J., Frost, C., Holden, P. (2000). Chemical weathering in the foreland of a retreating glacier. Geochimica et Cosmochimica Acta, 64(7), 1173–1189.

Askaer, L., Schmidt, L., Elberling, B., Asmund, G., & Jónsdóttir, I. (2008). Environmental Impact on an Arctic Soil–Plant System Resulting from Metals Released from Coal Mine Waste in Svalbard (78° N). Water, Air, and Soil Pollution, 195(1), 99–114.

Brooks, P.D., Schmidt, S.K., Williams, M.W. (1997). Winter production of CO2 and N2O from alpine tundra: environmental controls and relationship to inter-system C and N fluxes. ecologia 110, 403–413.

Cathro, R.J., Carne, R.C. (1982) Sedimentary exhalative (sedex) zinc-lead-silver deposits, northern Canadian Cordillera: CIM Bulletin, 75(840), 66–78.

Chambers, S. D., and Chapin III, F. S. (2002). Fire effects on surface-atmosphere energy exchange in Alaskan black spruce ecosystems: implications for feedbacks to regional climate. Journal of Geophysical Research, 107(D1), FFR 1-1 - FFR 1-17.

Chapelle, F.H. (1993). Ground-water Microbiology and Geochemistry. Wiley, New York, 424 pp. Elberling, B., Schippers, A., & Sand, W. (2000). Bacterial and chemical oxidation of pyritic mine tailings at low temperatures. Journal of Contaminant Hydrology, 41(3), 225–238.

Dai, B., Zhang, Y., Ding, H., Xu, Y., & Liu, Z. (2022). Characteristics and Prediction of the Thermal Diffusivity of Sandy Soil. Energies (Basel), 15(4), 1524–.

Duk-Rodkin, A. and Hughes, O.L., (1995). Quaternary geology of the northeastern part of the central Mackenzie Valley corridor, District of Mackenzie, Northwest Territories. Geological Survey of Canada, Bulletin 458.

EBA Engineering Consultants Ltd. (1990). Granular evaluation, Dempster Highway corridor, YT and NWT. Report to Department of Indian and Northern Affairs, Whitehorse, Yukon.

Elberling, B. (2001). Environmental controls of the seasonal variation in oxygen uptake in sulfidic tailings deposited in a permafrost-affected area. Water Resources Research, 37(1), 99–107.

Elberling, B. (2005). Temperature and oxygen control on pyrite oxidation in frozen mine tailings. Cold Regions Science and Technology, 41(2), 121–133.

Emsbo, P., Seal, R.R., Breit, G.N., Diehl, S.F., Shah, A.K. (2010). Mineral Deposit Models for Resource Assessment: Sedimentary Exhalative (SEDEX) Zinc-Lead-Silver Deposit Model. Scientific Investigations Report 2010-5070-N, U.S. Geological Survey.

Environment Canada, 2004. Canadian climate normals 1971–2001. Canada Atmospheric Environment Service. Minister of Supply and Services Canada, Ottawa, Ontario.

Fahnestock, J.T., Jones, M.H., Brooks, P.D., Walker, D.A., Welker, J.M., 1998. Winter and early spring CO2 efflux from tundra communities of northern Alaska. J. Geophys. Res. 103, 29023 – 29027.

Farquharson, L. M., Romanovsky, V. E., Kholodov, A., & Nicolsky, D. (2022). Sub-aerial talik formation observed across the discontinuous permafrost zone of Alaska. Nature Geoscience, 15(6), 475–481.

Fredlund, D., Fredlund, M., & Rahardjo, H. (2012). Unsaturated Soil Mechanics in Engineering Practice. Wiley-Interscience.

Fisher, D., Lacelle, D., Pollard, W. (2020a). A model of unfrozen water content and its transport in icy permafrost soils: Effects on ground ice content and permafrost stability. Permafrost and Periglacial Processes, 31(1), 184–199.

Fisher, D., Lacelle, D., Pollard, W., Faucher, B. (2020b). A model for stable isotopes of residual liquid water and ground ice in permafrost soils using arbitrary water chemistries and soil-specific empirical residual water functions. Permafrost and Periglacial Processes.

French H.M. (2017) The Northern Interior Yukon: An Example of Periglaciation. In: Slaymaker O. (eds) Landscapes and Landforms of Western Canada. World Geomorphological Landscapes. Springer.

French, H. M. (2018). The periglacial environment (Fourth edition.). John Wiley & Sons, Inc.

Gardaz, J. (1997). Distribution of Mountain Permafrost, Fontanesses Basin, Valaisian Alps, Switzerland. Permafrost and Periglacial Processes, 8(1), 101–105.

Girard, I., Klassen, R.A., Laframboise, R.R. (2003). Sedimentology laboratory manual. Terrain Sciences Division. Geological Survey of Canada, Open File 4823, Ottawa. 134 pp.

Gray, J., Brown, R. (1979). Permafrost presence and distribution in the Chic-Chocs Mountains, Gaspésie, Québec. Géographie Physique et Quaternaire, 33(3-4), 299–316.

Gray, N. (1997). Environmental impact and remediation of acid mine drainage: a management problem. Environmental Geology (Berlin), 30(1), 62–71.

Goodfellow, W.D., Lydon, J.W., and Turner, R.J.W. (1993). Geology and genesis of stratiform sediment-hosted (SEDEX) zinc-lead-silver sulphide deposits, Mineral deposit modeling: Geological Association of Canada special paper 40, p. 201–251.

Gorbunov, A.P. (1978). Permafrost Investigations in High-Mountain Regions. Arctic and Alpine Research, 10(2), 283–294.

Heiri, O., Lotter, A.F., Lemcke, G., 2001. Loss on ignition as a method for estimating organic and carbonate content in sediments: reproducibility and comparability of results. Journal of Paleolim- nology 25, 101–110.

Hinkel, Paetzold, F., Nelson, F. E., & Bockheim, J. G. (2001). Patterns of soil temperature and moisture in the active layer and upper permafrost at Barrow, Alaska: 1993–1999. *Global and Planetary Change*, *29*(3), 293–309.

Holloway, J. & Lewkowicz, A. G. (2020). *Impacts of Forest Fire on Permafrost in the Discontinuous Zones of Northwestern Canada*. Université d'Ottawa / University of Ottawa.

Holloway, J., Lewkowicz, A., Douglas, T., Li, X., Turetsky, M., Baltzer, J., & Jin, H. (2020). Impact of wildfire on permafrost landscapes: A review of recent advances and future prospects. Permafrost and Periglacial Processes, 31(3), 371–382.

Ilyashuk, B., Ilyashuk, E., Psenner, R., Tessadri, R., Koinig, K. (2018). Rock glaciers in crystalline catchments: Hidden permafrost-related threats to alpine headwater lakes. Global Change Biology, 24(4), 1548–1562.

Jacobs, J., Lehr, J., Testa, S. (2014). Acid mine drainage, rock drainage, and acid sulfate soils: causes, assessment, prediction, prevention, and remediation. WILEY.

Janke, J. (2005). The occurrence of alpine permafrost in the Front Range of Colorado. Geomorphology (Amsterdam, Netherlands), 67(3), 375–389.

Jennings, S.R., Neuman, D.R., and Blicker, P.S., 2008. Acid Mine Drainage and Effects on Fish Health and Ecology: A Review. Reclamation Research Group Publication, Bozeman, MT, 0-26.

Jafarov, E. E., Romanovsky, V. E., Genet, H., McGuire, A. D., and Marchenko, S. S. (2013). The effects of fire on the thermal stability of permafrost in lowland and upland black spruce forests of interior Alaska in a changing climate. Environmental Research Letters, 8(3), 035030.

Jorgenson, M., Romanovsky, V., Harden, J., Shur, Y., O'Donnell, J., Schuur, E., Kanevskiy, M., & Marchenko, S. (2010). Resilience and vulnerability of permafrost to climate change. Canadian Journal of Forest Research, 40(7), 1219–.

Jorgenson, T, Harden, J., Kanevskiy, M., O'Donnell, J., Wickland, K., Ewing, S., Manies, K., Zhuang, Q., Shur, Y., Striegl, R., & Koch, J. (2013). Reorganization of vegetation, hydrology and soil carbon after permafrost degradation across heterogeneous boreal landscapes. Environmental Research Letters, 8(3), 1–13.

Kwong, Y., Whitley, G., & Roach, P. (2009). Natural acid rock drainage associated with black shale in the Yukon Territory, Canada. Applied Geochemistry, 24(2), 221–231.

Kokelj, S.,Burn, C. (2005). Near-surface ground ice in sediments of the Mackenzie Delta, Northwest Territories, Canada. Permafrost and Periglacial Processes, 16(3), 291–303.

Kokelj, S., Lacelle, D., Lantz, T., Tunnicliffe, J., Malone, L., Clark, I., Chin, K. (2013). Thawing of massive ground ice in mega slumps drives increases in stream sediment and solute flux across a range of watershed scales. Journal of Geophysical Research. Earth Surface, 118(2), 681–692.

Kokelj, S., Jorgenson, M. (2013). Advances in Thermokarst Research. Permafrost and Periglacial Processes, 24(2), 108–119.

Kutiel, P., Lavee, H., Ackermann, O. (1998). Spatial distribution of soil surface coverage on north and south facing hillslopes along a Mediterranean to extreme arid climatic gradient. Geomorphology 23, 245–256.

Lacelle, D., Vasil'chuk, Y.K. (2013). Recent Progress (2007–2012) in Permafrost Isotope Geochemistry. Permafrost and Periglaclacial Processes, 24, 138-145.

Langdahl, B., Ingvorsen, K. (1997). Temperature characteristics of bacterial iron solubilisation and 14C assimilation in naturally exposed sulfide ore material at Citronen Fjord, North Greenland (83°N). FEMS Microbiology Ecology, 23(4), 275–283.

Langman, J., Veeramani, H., Blowes, D., Bailey, B., Wilson, D., Smith, L., Sego, D., Amos, R., & Holland, S. (2017). Waste Rock Biogeochemistry in a Permafrost Environment: Examination of a Cover Design for a Low-Sulfide, Granitic Waste Rock. Geomicrobiology Journal, 34(8), 656–669.

Lantz, T.C. & Kokelj, S.V. (2008). Increasing rates of retrogressive thaw slump activity in the Mackenzie Delta region, N.W.T., Canada. Geophysical Research Letters, 35(6), L06502–n/a.

Meldrum, J., Jamieson, H., Dyke, L. (2001). Oxidation of mine tailings from Rankin Inlet, Nunavut, at subzero temperatures. Canadian Geotechnical Journal, 38(5), 957–966.

Lessard, F., Bussière, B., Côté, J., Benzaazoua, M., Boulanger-Martel, V., & Marcoux, L. (2018). Integrated environmental management of pyrrhotite tailings at Raglan Mine: Part 2 desulphurized tailings as cover material. Journal of Cleaner Production, 186, 883–893.

Loranty, M., Abbott, B., Blok, D., Douglas, T., Epstein, H., Forbes, B., Jones, B., Kholodov, A., Kropp, H., Malhotra, A., Mamet, S., Myers-Smith, I., Natali, S., O'Donnell, J., Phoenix, G., Rocha, A., Sonnentag, O., Tape, K., & Walker, D. (2018). Reviews and syntheses: Changing ecosystem influences on soil thermal regimes in northern high-latitude permafrost regions. Biogeosciences, 15(17), 5287–5313.

Marinova, McKay, C. P., Heldmann, J. L., Goordial, J., Lacelle, D., Pollard, W. H., & Davila, A. F. (2022). Climate and energy balance of the ground in University Valley, Antarctica. *Antarctic Science*, *34*(2), 144–171.

Marion, G., Mironenko, M., & Roberts, M. (2010). FREZCHEM: A geochemical model for cold aqueous solutions. Computers & Geosciences, 36(1), 10–15.

McBride, M.B. (1994). Environmental Chemistry of Soils. Oxford University Press, New York, USA. 416 pp.

Mcguinness, Trodahl, H. J., Collins, K., & Haskell, T. G. (1998). Non-linear thermal transport and brine convection in first-year sea ice. Annals of Glaciology, 27, 471–476.

Michel, F.A. (1983). Isotope variations in permafrost waters along the Dempster Highway pipeline corridor. Permafrost, Proceedings of the 4th International Conference, Fairbanks, Alaska, July 1983, (1) 843-848.

Murray, D.W. (1997). Ecological summary of Eagle Plains Park candidate areas, cross-section and report. Yukon Department of Renewable Resources, Government of the Yukon, Whitehorse, Yukon.

Nelson, J.L., Paradis, S., Christensen, J., Gabites, J. (2002). Canadian Cordilleran Mississippi Valley- type deposits—A case for Devonian-Mississippian back-arc hydrothermal origin: Economic Geology, v. 97, no. 5, p. 1013–1036.

Nordstrom, D.K., Southam, G. (1997). Geomicrobiology of sulfide mineral oxidation. In: Banfield, J.F., Nealson, K.H., (Eds.), Geomicrobiology: Interactions Between Microbes and Minerals. Reviews in Mineralogy, 35, 361–390.

Norris, D.K. (1975). Geology of Eagle River, 1:250,000. Map 1523A, Geological Survey of Canada, Ottawa, Canada.

Nossov, D. R., Jorgenson, M. T., Kielland, K., and Kanevskiy, M. Z. (2013). Edaphic and microclimatic controls over permafrost response to fire in interior Alaska. Environmental Research Letters, 8(3), 035013.

O’Donnell, J. A., Jorgenson, M. T., Harden, J. W., McGuire, A. D., Kanevskiy, M. Z., Wickland, K. P. (2012). The effects of permafrost thaw on soil hydrologic, thermal, and carbon dynamics in an Alaskan Peatland. Ecosystems, 15, 213-229.

Pettorelli, N. (2013). The normalized difference vegetation index (First edition.). Oxford University Press. 194p.

Price, W.A. (2005). List of Potential Information Requirements in Metal Leaching/Acid Rock Drainage Assessment and Mitigation Work. Report 5.01E. Mining Environment Neutral Drainage Program, Canada Centre for Mineral and Energy Technology, 0-25.

Riseborough, D.W. (2003). Thawing and freezing indices in the active layer. Permafrost 8th International Conference, Permafrost, Phillips, Springman & Arenson (eds).

Rouse, W. R. (1976). Microclimatic changes accompanying burning in subarctic lichen woodland. Arctic and Alpine Research, 8(4), 357-376.

Salerno, F., Rogora, M., Balestrini, R., Lami, A., Tartari, G., Thakuri, S., Godone, D., Freppaz, M., Tartari, G. (2016). Glacier Melting Increases the Solute Concentrations of Himalayan Glacial Lakes. Environmental Science & Technology, 50(17), 9150–9160.

Schoonen, M., Elsetinow, A., Borda, M., & Strongin, D. (2000). Effect of temperature and illumination on pyrite oxidation between pH 2 and 6. Geochemical Transactions GT, 1(1), 1–11.
Séjourné, A., Costard, F., Fedorov, A., Gargani, J., Skorve, J., Massé, M., & Mège, D. (2015). Evolution of the banks of thermokarst lakes in Central Yakutia (Central Siberia) due to retrogressive thaw slump activity controlled by insolation. Geomorphology (Amsterdam, Netherlands), 241, 31–40.

Shiklomanov, N. & Nelson, F. (1999). Analytic representation of the active layer thickness field, Kuparuk River Basin, Alaska. Ecological Modelling, 123(2), 105–125.

Siegel, F.R. (2002). Environmental Geochemistry of Potentially Toxic Metals. Springer-Verlag, Berlin. 218 pp.

Skovsholt, L., Pastor, A., Docherty, C., Milner, A., & Riis, T. (2020). Changes in hydrology affects stream nutrient uptake and primary production in a high-Arctic stream. Biogeochemistry, 151(2- 3), 187.

Smith, S.L., Burgess, M.M., (2000). Ground temperature database for northern Canada. Geological Survey of Canada, Open File Report 3954.

Smith, C.A.S., Meikle, J.C., Roots, C.F. (editors), 2004. Ecoregions of the Yukon Territory: Biophysical properties of Yukon landscapes. Agriculture and Agri-Food Canada, PARC Technical Bulletin No. 04-01, Summerland, British Columbia, 313 p.

Smith, M.W. & Riseborough, D. W. (2002). Climate and the limits of permafrost: a zonal analysis. *Permafrost and Periglacial Processes*, *13*(1), 1–15.

Smith, S. L., Riseborough, D. W., & Bonnaventure, P. P. (2015). Eighteen Year Record of Forest Fire Effects on Ground Thermal Regimes and Permafrost in the Central Mackenzie Valley, NWT, Canada: Eighteen Year Record of the Effects of Forest Fire on Ground Thermal Regimes. Permafrost and Periglacial Processes, 26(4), 289–303.

Sulman, S., V. G., Iversen, C. M., Breen, A. L., Yuan, F., & Thornton, P. E. (2021). Integrating Arctic Plant Functional Types in a Land Surface Model Using Above- and Belowground Field Observations. *Journal of Advances in Modeling Earth Systems*, *13*(4).

Thomas, R.D. and Rampton, V.N., 1982. Surficial geology and geomorphology; North Klondike River, Yukon Territory. Geological Survey of Canada, map 6-1982, scale 1:100,000.

Trodahl, McGuinness, M. J., Langhorne, P. J., Collins, K., Pantoja, A. E., Smith, I. J., & Haskell, T. G. (2000). Heat transport in McMurdo Sound first-year fast ice. Journal of Geophysical Research, 105(C5), 11347–11358.

Trodahl, Wilkinson, S. O. F., McGuinness, M. J., & Haskell, T. G. (2001). Thermal conductivity of sea ice; dependence on temperature and depth. Geophysical Research Letters, 28(7), 1279–1282.

Unterweger, M., Coursey, B., Schima, F., & Mann, W. (1980). Preparation and calibration of the 1978 National Bureau of Standards tritiated-water standards. The International Journal of Applied Radiation and Isotopes, 31(10), 611–614.

van Deventer, H., & Cho, M. (2014). Assessing leaf spectral properties of Phragmites australis impacted by acid mine drainage. South African Journal of Science, 110(7/8), 1–12.

Williams, P. (1968). Ice distribution in permafrost profiles. Canadian Journal of Earth Sciences, 5(6), 1381–1386.

Williams, P., Smith, M. (1989). The frozen earth : fundamentals of geocryology. Cambridge University Press.

Zhang, & Osterkamp, T. E. (1995). Considerations in determining thermal diffusivity from temperature time series using finite difference methods. Cold Regions Science and Technology, 23(4), 333–341.

Appendix 1: Active layer geochemistry

Table 5. Active layer pH and soluble ion concentrations (mg/L) at AS1.

Sample	Depth	pH	Al_{tot}	Ca^{2+}	Fe_{tot}	K^+	Mg^{2+}	Mn_{tot}	Na^+	Ni^{2+}	Zn^{2+}	Cl^-	SO_4^{2-}	NO_3^-	TDS
AS-01	0 - 5	3.3	0.12	3.82	1.64	3.25	0.63	0.03	5.38	0.01	0.90	4.30	248.12	0.86	269.06
AS-02	5 - 10	2.9	2.21	9.35	13.51	1.47	1.64	0.08	7.73	0.02	0.98	4.07	719.92	1.47	762.45
AS-03	10 - 15	2.9	5.41	17.26	22.29	1.79	4.87	0.18	8.70	0.08	0.73	3.51	1293.37	0.56	1358.75
AS-04	15 - 20	2.8	7.30	19.70	25.23	0.98	6.49	0.21	6.45	0.06	0.52	3.31	1382.71	0.44	1453.40
AS-05	20 - 25	2.9	7.23	16.49	22.02	1.41	6.37	0.20	7.33	0.07	0.65	4.41	1194.66	0.72	1261.56
AS-06	25 - 30	2.7	18.41	30.74	59.81	0.93	10.48	0.33	7.91	0.16	0.83	9.37	2116.69	0.89	2256.55
AS-07	30 - 35	2.5	35.61	51.16	120.22	2.21	14.68	0.45	16.98	0.29	1.01	29.80	3566.32	1.02	3839.76
AS-08	35 - 40	2.7	15.75	26.07	42.23	0.75	6.16	0.20	11.73	0.16	0.99	6.14	1654.40	1.83	1766.42
AS-09	40 - 45	2.7	25.75	31.12	65.39	0.47	4.28	0.19	6.59	0.20	1.75	10.08	1917.81	0.64	2064.26
AS-10	45 - 50	2.6	40.05	42.52	102.31	1.96	6.75	0.26	10.61	0.25	3.23	15.26	2498.81	1.51	2723.52
AS-11	50 - 55	2.7	25.04	32.86	59.93	0.54	5.78	0.21	6.94	0.20	1.23	5.99	1671.95	0.56	1811.24
AS-12	55 - 60	2.9	12.57	28.62	31.49	0.23	6.12	0.22	5.63	0.16	0.93	2.72	1237.57	0.47	1326.74
AS-13	60 - 65	2.9	19.89	45.11	44.82	0.36	9.38	0.31	8.83	0.30	1.31	3.05	1520.37	0.89	1654.62
AS-14	65 - 70	3	14.86	40.27	32.39	0.21	8.12	0.27	7.31	0.27	1.20	1.94	1440.86	0.40	1548.09
AS-15	70 - 75	2.9	18.06	48.98	35.96	0.28	10.67	0.34	7.87	0.34	1.07	1.86	1439.97	0.49	1565.88
AS-16	75 - 80	3	28.24	81.96	43.93	0.72	19.85	0.65	16.60	0.54	1.25	3.18	2047.87	1.16	2245.95
AS-17	80 - 85	3	25.23	66.75	43.76	0.96	14.95	0.52	14.55	0.50	1.09	2.79	1827.14	1.36	1999.59
AS-18	85 - 90	3	34.60	100.88	56.40	1.97	21.99	0.86	24.30	0.71	1.13	5.90	2572.67	2.08	2823.48
Average	-	2.86	18.69	38.54	45.74	1.14	8.85	0.31	10.08	0.24	1.16	6.54	1686.18	0.96	1818.41
St dev	-	0.19	11.72	25.03	29.37	0.84	5.78	0.20	5.01	0.19	0.59	6.73	736.10	0.50	802.99

Table 6. Active layer pH and soluble ion concentrations (mg/L) at AS2.

Sample	Depth	pH	Al_{tot}	Ca^{2+}	Fe_{tot}	K^+	Mg^{2+}	Mn_{tot}	Na^+	Ni^{2+}	Zn^{2+}	Cl^-	SO_4^{2-}	NO_3^-	TDS
AS2-01	0 - 5	3.7	3.58	51.02	7.33	2.50	5.59	0.29	3.32	0.20	0.94	1.93	435.10	0.29	512.09
AS2-02	5 - 10	2.9	3.57	12.68	17.17	0.81	2.03	0.10	4.38	0.05	0.57	3.26	889.87	0.45	934.93
AS2-03	10 - 15	3.3	6.70	78.31	8.95	1.75	6.68	0.32	3.87	0.32	1.20	1.63	708.11	0.63	818.47
AS2-04	15 - 20	3.2	7.95	118.18	10.77	2.86	13.94	0.52	10.91	0.36	1.10	1.78	903.72	0.63	1072.71
AS2-05	20 - 25	3.2	10.75	142.90	18.25	3.89	16.69	0.67	16.47	0.42	1.07	1.55	1214.13	0.96	1427.75
AS2-06	25 - 30	3.2	11.77	127.63	14.72	1.75	14.99	0.58	11.36	0.42	1.29	1.41	1048.51	0.58	1235.01
AS2-07	30 - 35	3.3	17.08	184.26	12.57	2.57	21.25	0.82	15.80	0.58	1.18	1.88	1336.47	0.72	1595.16
AS2-08	35 - 40	3.4	24.38	247.86	7.28	2.93	28.17	1.12	22.02	0.84	1.48	2.88	1440.75	0.55	1780.26
AS2-09	40 - 45	3.8	27.20	236.73	1.42	1.37	25.24	1.06	12.96	1.46	2.09	1.67	921.06	1.06	1233.33
AS2-10	45 - 50	4.2	20.56	204.61	0.58	11.69	21.37	0.96	21.79	1.49	2.39	8.30	677.49	6.26	977.49
AS2-11	50 - 55	4.2	37.47	406.38	0.94	1.00	41.21	1.81	20.57	2.82	2.87	1.83	1405.02	0.27	1922.19
AS2-12	55 - 60	4.4	27.99	362.48	0.71	1.77	33.09	1.48	14.42	2.51	2.67	1.12	1183.39	-0.05	1631.58
AS2-13	60 - 65	4.3	22.30	330.76	0.74	3.73	30.94	1.26	13.07	2.08	2.33	1.07	1061.38	0.26	1469.92
AS2-14	65 - 70	4.3	16.07	285.99	0.92	4.03	25.38	0.88	15.23	1.54	2.04	2.09	903.56	1.03	1258.77
AS2-15	70 - 75	4.2	16.20	277.50	4.82	8.68	23.54	0.92	11.77	1.35	1.79	1.30	935.72	0.58	1284.18
AS2-16	75 - 80	3.9	19.72	355.34	1.62	5.63	30.45	1.13	12.07	1.53	2.12	1.40	1276.88	0.23	1708.12
AS2-17	80 - 85	3.6	14.46	245.80	2.60	3.77	22.72	0.86	11.50	0.99	2.09	1.64	1005.07	1.37	1312.86
Average	-	3.71	16.93	215.79	6.55	3.57	21.37	0.87	13.03	1.11	1.72	2.16	1020.37	0.93	1304.40
St dev	-	0.49	9.25	115.29	6.19	2.84	10.44	0.44	5.62	0.83	0.67	1.68	271.12	1.42	369.01

Table 7. Active layer pH and soluble ion concentrations (mg/L) at NAS1 and NAS2

Sample	Depth	pH	Al_{tot}	Ca^{2+}	Fe_{tot}	K^+	Mg^{2+}	Mn_{tot}	Na^+	Ni^{2+}	Zn^{2+}	Cl^-	SO_4^{2-}	NO_3^-	TDS
NAS-01	10 - 15	4.8	11.47	18.21	20.35	56.08	4.01	0.25	24.13	0.10	0.42	10.93	59.53	7.70	213.18
NAS-02	20 - 25	5.1	12.66	39.12	93.33	30.68	8.27	0.33	30.46	0.18	0.41	9.25	84.23	8.76	317.69
NAS-03	30 - 35	4.7	32.22	53.77	19.86	15.20	14.03	0.64	40.97	0.13	0.44	8.69	185.81	10.14	381.90
NAS-04	40 - 45	5.5	28.40	72.43	32.65	13.62	19.54	0.69	42.57	0.09	0.38	8.03	187.87	-0.10	406.18
Average	-	5.03	21.19	45.88	41.55	28.89	11.46	0.48	34.53	0.13	0.42	9.23	129.36	6.62	329.74
St dev	-	0.36	10.66	22.94	35.02	19.69	6.77	0.22	8.77	0.04	0.03	1.24	67.14	4.60	86.21
NAS2-01	10 - 15	4.4	2.36	3.71	2.23	44.80	0.87	0.06	5.58	-0.01	0.23	14.40	17.48	-0.03	91.69
NAS2-02	25 - 30	4.9	19.90	28.06	17.97	44.88	8.51	0.29	21.94	0.08	0.38	15.08	75.65	3.32	236.08
Average	-	4.65	11.13	15.89	10.10	44.84	4.69	0.18	13.76	0.03	0.31	14.74	46.57	1.65	163.88
St dev	-	0.35	12.40	17.22	11.13	0.06	5.40	0.16	11.57	0.07	0.11	0.48	41.13	2.37	102.10